

Deformation and breakup of bubbles and drops in turbulence

Rui Ni¹

¹Department of Mechanical Engineering, The Johns Hopkins University, Baltimore, MD 21218, USA; email: rui.ni@jhu.edu

Xxxx. Xxx. Xxx. Xxx. 2023. AA:1–30

[https://doi.org/10.1146/\(\(please add article doi\)\)](https://doi.org/10.1146/((please add article doi)))

Copyright © 2023 by the author(s).
All rights reserved

Keywords

turbulent multiphase flow, deformation and breakup/fragmentation, emulsion, polydispersed droplets and bubbles, lift and drag, heat and mass transfer

Abstract

Fragmentation of bubbles and droplets in turbulence produces a dispersed phase spanning a broad range of scales, encompassing everything from droplets in nanoemulsions to centimeter-sized bubbles entrained in breaking waves. Along with deformation, fragmentation plays a crucial role in enhancing interfacial area, with far-reaching implications across various industries, including food, pharmaceuticals, and ocean engineering. However, understanding and modeling these processes is challenging due to the complexity of anisotropic and inhomogeneous turbulence typically involved, the unknown residence time in regions with different turbulence intensities, and difficulties arising from the density and viscosity ratios. Despite these challenges, recent advances have provided new insights into the underlying physics of deformation and fragmentation in turbulence. This review summarizes existing works in various fields, highlighting key results and uncertainties, and examining the impact on turbulence modulation, drag reduction, and heat and mass transfer.

1. Introduction

Mixing two immiscible fluids (gas-liquid or liquid-liquid) in turbulence produces polydispersed droplets or bubbles that can freely deform, break, and coalesce while interacting with the surrounding turbulence. These processes are fundamentally important and practically relevant to multiple fields, including bubble-mediated air-sea mass exchange (Villermaux et al. 2022), chemical emulsions, food science, nuclear thermal hydraulics, and two-phase heat transfer. In contrast to the deformation and breakup of droplets in low-Reynolds-number viscous flows (Stone 1994), in turbulence, these dynamics are intimately linked to multiple length and time scales associated with the background turbulent eddies.

A wide range of drop/bubble sizes can therefore be achieved via the adjustment of the turbulence characteristics. For example, turbulence generated by a simple batch stirrer system can break an oil-water mixture into macroemulsions with the size of the dispersed oil droplets at $\mathcal{O}(1\text{--}100\ \mu\text{m})$. But if nanoemulsions with droplets of $\mathcal{O}(10\text{--}100\ \text{nm})$ are desired, the turbulent scales have to be much smaller, requiring an energy-intensive high-pressure homogenizer (HPH) method (Schultz et al. 2004, Håkansson 2019).

Despite the wide range of scales involved, many key concepts crucial to understanding deformation and breakup in turbulence can be traced back to the seminal works by Kolmogorov (1949) and Hinze (1955), i.e. the Kolmogorov-Hinze (KH) framework. The KH framework has gained widespread acceptance in various fields, however, it is crucial to acknowledge that it contains a number of assumptions and hypotheses. The purpose of this review is to gather studies from various disciplines that investigate the deformation and breakup of both droplets and bubbles in turbulence, in order to determine the regimes in which the KH framework is applicable and more importantly, where it may fall short and new challenges and opportunities await.

Key hypotheses and assumptions in the Kolmogorov-Hinze framework

(a) Turbulence was assumed to be homogeneous and isotropic. (b) The drop size was assumed to be in the inertial range of turbulence. (c) Droplets were assumed to be neutrally buoyant, with buoyancy and density ratio disregarded. (d) It was hypothesized that the breakup is driven by the dynamic pressure caused by changes in velocity over distances at the most equal to the drop diameter. (e) The framework assumes that the interaction between drops and turbulence is one-way, with droplets having no effect on the turbulent dynamics. (f) While Kolmogorov took into account the kinematic viscosity ratio between the two phases to separate different regimes, Hinze proposed to use the Ohnesorge number (defined in Section 2) to measure the importance of the inner viscosity.

This review provides an overview of the dynamics of deformation and breakup and their impacts on momentum, mass, and heat transfer, with a particular focus on experimental methods and results and a limited survey of simulation findings. For in-depth coverage of numerical methods for resolving deformable interfaces in turbulence, readers are referred to the recent reviews by Tryggvason et al. (2013) and Elghobashi (2019). The subject is closely related to the broader realm of particle-laden turbulence, including spherical (Balachandar & Eaton 2010, Brandt & Coletti 2022), non-spherical (Voth & Soldati 2017), and buoyant particles (Mathai et al. 2020), but with a particular emphasis on deformability. This review also complements other comprehensive reviews on fragmentation (Villermaux

2007), bubble dynamics (Magnaudet & Eames 2000, Risso 2018, Lohse 2018), and the complexity introduced by surfactant (Takagi & Matsumoto 2011), phase inversion (Bakhuizen et al. 2021), and non-Newtonian liquids (Zenit & Feng 2018).

The problem being considered involves bubbles and droplets of a specific diameter, denoted as D , being deformed and fragmented by surrounding turbulence characterized by parameters, such as energy dissipation rate (ϵ), fluctuation velocity (u'), integral scale (L), and the Kolmogorov scale (η). The density, dynamic and kinematic viscosities are denoted by ρ , μ , and ν , respectively. The fluid properties of the carrier phase and dispersed phase can be differentiated using subscripts c and d , respectively. The interfacial tension between the two phases is represented by σ .

The problem at hand is characterized by a multitude of parameters, and as a result, the relevant dimensionless groups are also vast. However, by making some key assumptions and hypotheses, as outlined in **Textbox 1**, Kolmogorov (1949) was able to simplify the problem. He proposed that, for the deformation and breakup of large bubbles/droplets ($\eta \ll D \ll L$), the most important dimensionless number is the Weber number, which is a measure of the ratio between the inertial forces to surface tension forces.

$$We_t = \frac{\rho_c u_D^2 D}{\sigma} \quad 1.$$

where u_D is the eddy velocity of size D and $u_D^2 = C_2(\epsilon D)^{2/3}$ is the estimation using the second-order structure function in the inertial range in homogeneous and isotropic turbulence (HIT), where $C_2 \approx 2.3$ is the Kolmogorov constant. Furthermore, it was postulated that, if the Weber number is the only dimensionless number that affects the breakup problem, there must exist a critical Weber number (We_t^c) that corresponds to the critical diameter (D^c), below which the droplets remain stable for a prolonged period in turbulence.

$$D^c = \left(\frac{We_t^c \sigma}{\rho_c C_2 \epsilon^{2/3}} \right)^{3/5} \quad 2.$$

The idea of a critical Weber number implies an abrupt shift from a finite breakup probability to zero at We_t^c , a simplistic view which does not account for turbulent fluctuations. Although the likelihood of eddies with local energy dissipation rates significantly higher than the mean is low, it is not zero. Therefore, even if the mean Weber number is below We_t^c , the occasional high-energy eddies can still break bubbles or droplets. Additionally, while We_t captures the contribution of turbulence, persistent large-scale forcing, such as shear or buoyancy, can aid and even dominate deformation and breakup. To understand the fundamental breakup mechanisms, their contributions must be distinguished from those of turbulence. Lastly, incorporating the effects of viscosity poses significant challenges, requiring a systematic review of existing experimental data. To this end, this review is structured as follows. In Section 2, different regimes of deformation and breakup driven by turbulence, including the effects of large-scale forcing and viscous damping, are reviewed. Section 3 provides an overview of the key results and models of breakup frequency. In Section 4, the findings on how deformation and breakup influence the momentum, heat, and mass transfer between phases are summarized.

2. Various breakup Regimes

Figure 1 illustrates the relevant regimes that have been studied and the typical deformation and breakup morphology that has been observed. **Figure 1a** emphasizes the problems

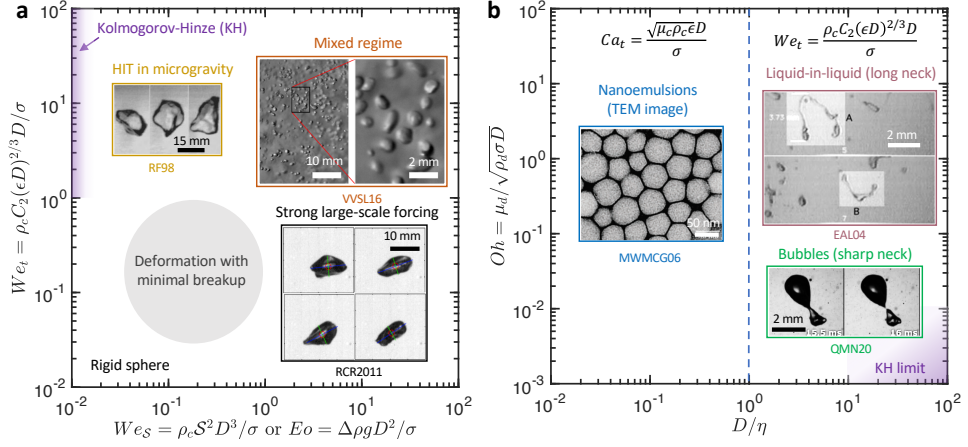


Figure 1

A parameter space of deformation and breakup of bubbles/droplets in turbulence characterized by (a) the Weber number defined based on the small-scale turbulence (We_t) versus large-scale persistent forcing measured by either shear (We_S) or buoyancy (Eo), and (b) the Ohnesorge number (Oh) and the size of the bubbles/drops (D) relative to the Kolmogorov scale (η). The inset panels are adapted with permission from RF98 (Risso & Fabre 1998), VVSL16 (Verschoof et al. 2016), RCR2011 (Ravelet et al. 2011), MWMCG06 (Mason et al. 2006), EAL04 (Eastwood et al. 2004), and QMN20 (Qi et al. 2020). The placement of these insets in the parameter space only indicates the general regimes they correspond to, not their exact parameters.

dominated by inertia but separately considers the effects of small-scale turbulence (We_t) and large-scale forcing. The large-scale forcing can arise in various forms, including a persistent mean shear with the shear rate denoted as S and a pressure gradient induced by buoyancy-driven migration, with their roles in deformation measured by the shear Weber number $We_S = \rho_c S^2 D^3 / \sigma$ and the Eötvös or Bond number $Eo = \Delta \rho g D^2 / \sigma$, respectively.

Figure 1b emphasizes the transition from an inertia-dominated to a viscous-dominated regime when D crosses the Kolmogorov length scale ($\eta = (\nu_c^3 / \epsilon)^{1/4}$) and the viscous effect becomes more pronounced. In the viscous regime, the crucial dimensionless number is the Capillary number, i.e. $Ca_t = \sqrt{\mu_c \rho_c \epsilon} D / \sigma$. As the viscous effect of the outer fluid becomes relevant, it is also necessary to consider the regimes when the inner viscosity matters as well. As a result, another key dimensionless number, i.e. the Ohnesorge number ($Oh = \mu_d / \sqrt{\rho_d \sigma D}$), is considered to measure the relative significance of μ_d in resisting and damping deformation.

2.1. Inertia-dominated regime ($D > \eta$)

2.1.1. Intense homogeneous and isotropic turbulence ($We_t > Eo$ and $We_t > We_S$).

In this regime, the classical KH framework is most applicable. However, it can be difficult to achieve these ideal conditions in experiments. In closed systems, HIT can be generated by forcing flows from multiple symmetrical locations. As these flows merge, HIT can be produced near the center, where it is farthest from the momentum sources and therefore has

the lowest energy dissipation rate. This location is also where measurements were typically taken. As a result, the probability of breakup is much higher outside the measurement volume than inside. Bubbles and drops that are likely to break would have already been broken before entering the measurement volume, making it challenging to study their behavior in classical HIT systems.

One solution is to use HIT that decays along one direction and guide bubbles or droplets through turbulence along the opposite direction. In this way, the energy dissipation rate that bubbles/drops encounter continues to increase and the measurement volume can be set at a location where the energy dissipation rate is the highest but the flow is still HIT. Masuk et al. (2019b) designed a vertical water tunnel with a jet array located at the top of the test section and firing jets co-axially with the mean flow downward into the test section. The facility and its key dimensions are shown in **Figure 2a**. Tan et al. (2023) showed that, in this facility, the flow becomes HIT at around six nozzle spacings below the jet array, and such HIT continues to decay. The decay was found to scale with the nozzle diameter (d_n) and the jet velocity at the nozzle exit (v_j). In particular, the fluctuation velocity follows $u'/v_j = (x/d_n)^{-1}$, and the energy dissipation rate decays as $\epsilon/(v_j^3/d) = 0.76(x/d)^{-7/2}$. In this setup, the bubbles were injected at the bottom of the test section where the energy dissipation rate is the weakest. As they rise, the turbulence intensity grows, and eventually reaches a point where it is sufficient to cause bubbles to deform and break. Turbulence at this location, where the measurement volume is also placed, features large energy dissipation rates of $\mathcal{O}(1) \text{ m}^2/\text{s}^3$, which is sufficient for bubbles of size $\mathcal{O}(1) \text{ mm}$ to reach the condition of $We_t > Eo$.

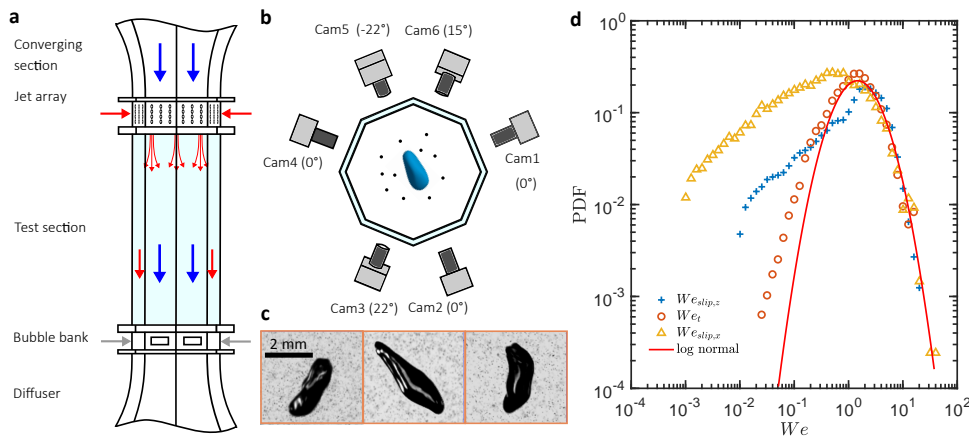


Figure 2

(a) Schematic of the side view of a vertical water tunnel that uses a jet array to produce intense HIT to study deformation and breakup (Masuk et al. 2019b, Qi et al. 2020). (b) The top view of the octagonal test section along with six cameras that were used to measure the shape of deformed bubbles simultaneously with the nearby 3D turbulence (Masuk et al. 2019a, Qi et al. 2020). (c) Examples of one strongly-deformed bubble captured by three different cameras. (d) The distribution of the Weber number defined based on different velocities. The red line indicates the log-normal distribution predicted based on the distribution of the instantaneous energy dissipation rate (Masuk et al. 2021c).

Apart from increasing turbulence intensity, another approach to reach $We_t > Eo$ is to

Slip velocity: the instantaneous velocity difference between the two phases. This quantity is different from the mean slip velocity used in atomization.

weaken the buoyancy effect. Risso & Fabre (1998) conducted experiments in a parabolic flight, reducing the gravitational constant to $g = 0.4 \text{ m/s}^2$ and effectively reducing EO by 25 times. In this experiment, turbulence was generated via an axisymmetrical momentum jet close to the bottom of the device (Risso & Fabre 1997). The average size of bubbles investigated is about 18 mm, which would have broken due to buoyancy alone if the experiments were conducted under the Earth’s gravity (Tripathi et al. 2015), but under microgravity, the buoyancy effect was much weaker, and breakup was dominated by turbulence. One sequence of images for strongly-deformed bubble in such an environment is shown in an inset of **figure 1a**. The critical Weber number averaged over all the cases was reported to be around 4.5. A numerical version of the same experiment was conducted by Qian et al. (2006) using the lattice Boltzmann method with bubbles being fragmented in homogeneous turbulence in a three-dimensional periodic box. The reported critical Weber number was around 3.

Although microgravity helps reduce the impact of the relative motion between the two phases (slip velocity) driven by buoyancy, this rising motion is not the sole source of the additional pressure gradient that could drive deformation. Even with a neutrally-buoyant dispersed phase, as assumed in the KH framework, slip velocity (u_{slip}) cannot be fully eliminated due to finite size effects (Homann & Bec 2010, Bellani & Variano 2012). To determine the extent to which deformation is driven by slip velocity, Masuk et al. (2021c) conducted an experiment to measure the shape of deforming bubbles simultaneously with their surrounding turbulence in 3D. This challenging experiment was accomplished using a diagnostic setup, which included six cameras positioned around the test section (**figure 2b**). Typical images of a deformed bubble, along with the nearby tracers, are shown in **figure 2c**. The shadows of high concentration of tracers were tracked using the openLPT method (Tan et al. 2020), while the bubble geometry was reconstructed using a technique that employs surface tension as an additional physical constraint, resulting in improved reconstruction quality (Masuk et al. 2019a).

These simultaneous measurements provide insight into the Lagrangian evolution of the bubble Weber number and the shape of individual bubbles (Masuk et al. 2021c). The distributions of the Weber number based on different velocity scales are shown in **figure 2d**. $We_t = \rho(\widetilde{\lambda}_3 D)^2 D / \sigma$, in this case, was determined by using the eigenvalue, λ_3 , that corresponds to the most compressive direction (\hat{e}_3), of the strain rate tensor coarse-grained at the bubble scale. The ensemble average of this definition of We_t should be equivalent to the one proposed in the KH framework, but it provides a more accurate representation of the relevant instantaneous Weber number, which was confirmed by the fact that the semi-minor axis of the bubble preferentially aligns with \hat{e}_3 . This alignment suggests that it is the converging flow near the bubble and the resulting pressure rise on the interface that leads to compression and deformation. The PDF of We_t can be captured through a log-normal distribution (red line in **figure 2d**), calculated by following the definition of We_t and the distribution of local energy dissipation rate that is described by the refined Kolmogorov theory (Kolmogorov 1962) and the multi-fractal spectrum (Meneveau & Sreenivasan 1991).

In addition to the strain rate, the instantaneous slip velocity was also calculated and divided into the horizontal (x) and vertical components (z). Their respective Weber numbers, i.e. $We_{\text{slip},x}$ and $We_{\text{slip},z}$, can be calculated by using the slip velocity as the velocity scale. The PDF of $We_{\text{slip},z}$ contains the contribution by the buoyancy-driven deformation, but the overall shapes of $We_{\text{slip},x}$ and $We_{\text{slip},z}$ remain similar to each other. The difference between $We_{\text{slip},x}$ and We_t (**figure 2d**), on the other hand, is significant, underscoring the difference

between two deformation mechanisms brought by turbulence and finite-sized bubbles.

Through simultaneous measurements, a simple relationship between We_t and aspect ratio of the bubble α , following $\alpha = 2We_t^{2/3}/5 + 1.2$, was determined by minimizing the difference between the PDF of α obtained from direct shape measurement and that calculated from We_t . This relationship provides a way to describe bubble deformation in turbulence, which complements studies that investigated the deformation of gas bubbles rising in quiescent liquids (Legendre et al. 2012). In turbulence, while it was noted that the fit against We_t is slightly better than against We_{slip} , the difference was not substantial, suggesting that both are important in bubble deformation. However, the orientation analysis by Masuk et al. (2021b) indicates that the bubble semi-minor axis aligns significantly better with the slip velocity than with \hat{e}_3 , emphasizing the crucial roles played by slip velocity in bubble deformation in turbulence.

2.1.2. Shear or buoyancy dominated deformation ($We_t < Eo$ or $We_t < We_S$).

2.1.2.1. Buoyancy dominated regime ($We_t < Eo$). In this regime, deformation is predominantly driven by buoyancy and the turbulence effect is minimal. Sevik & Park (1973) conducted an experiment on the breakup of bubbles in a turbulent jet. Bubbles with diameter varying from 4.0 mm to 5.8 mm were injected along the centerline of the jet. Eo ranges from 2.1 to 4.5, and the critical Weber number determined was about 1.3. This critical We_t is much smaller than 4.5 reported by Risso & Fabre (1998) based on the experiments conducted in microgravity, indicating less stress from turbulence was needed to break bubbles thanks to the extra help from buoyancy.

Ravelet et al. (2011) conducted an experiment of large bubbles rising in weak turbulence and reported two different Weber numbers, one based on the bubble's typical rise velocity and the other on the velocity gradient across the bubble. The fact that the former Weber number was close to 11.6 indicates that bubbles were strongly deformed due to buoyancy. The latter one, We_t as defined in equation 1, was around 1.8, which was about an order of magnitude smaller. **Figure 1a** displays snapshots of a deforming bubble, which show resemblance to bubbles rising in a still medium (Mougin & Magnaudet 2001), with the short axis of the bubble preferentially tilted towards the vertical direction and exhibiting periodic motions. These similarities were expected since bubbles were still primarily compressed in the vertical direction and the same wake instability occurred (Zenit & Magnaudet 2008). Despite these similarities, the time series of bubble deformation in turbulence were more chaotic and the decorrelation timescale was associated with the mode-2 natural frequency of the small-amplitude bubble oscillation, i.e. $f_2 = \sqrt{96\sigma/\rho_c D^3}$. The natural oscillation timescale was proposed as an important timescale by Sevik & Park (1973) and Risso & Fabre (1998) based on the physical picture of a bubble resonating with turbulent perturbations at its natural frequency. However, with strong buoyancy, Ravelet et al. (2011) suggested that the preferential sliding motion between the two phases significantly changes the deformation dynamics, leading to breakup driven by single intense eddies rather than the stochastic resonance observed under microgravity ($We_t > Eo$). This work implied that persistent deformation in one direction could alter the deformation dynamics driven by turbulence more than just adding to the stress.

2.1.2.2. Shear dominated regime ($We_t < We_S$). Levich (1962) considered the breakup of small drops immersed in the logarithmic sub-layer of a turbulent boundary layer (TBL).

The mean velocity parallel to the wall, $\langle U \rangle$, in the wall normal direction (y) is described by $\langle U \rangle = U_\tau \ln(y/y_0)/\kappa$, where $U_\tau = \sqrt{\tau_w/\rho_c}$ is the friction velocity and is determined by the wall shear stress (τ_w). The characteristic length scale is expressed as $\delta_0 = \nu_c/U_\tau$ and $y_0 = \delta_0/9$. $\kappa \approx 0.4$ is the von-Kármán constant. Levich (1962) argued that the pressure gradient that drives the drop deformation is dominated by the persistent large-scale shear across the drop size D from y to $y + D$. Assuming $d \ll y$, the Weber number (We_S) can be expressed as a function of y

$$We_S = \frac{2\rho_c U_\tau^2 D^2}{\kappa^2 y \sigma} \ln \frac{y}{y_0} \quad \text{and} \quad We_{S,\max} = \frac{\ln(180)\rho_c U_\tau^3 D^2}{10\kappa^2 \nu_c \sigma} \approx \frac{3\rho_c U_\tau^3 D^2}{\kappa^2 \nu_c \sigma} \quad 3.$$

where $We_{S,\max}$ is the largest value of We_S that can be reached near the bottom end of the log layer ($y \approx 20\delta_0$). Equation 3 is slightly different from the original work by Levich (1962) after I corrected some issues, e.g. the assumption of the bottom of the log layer at $y \approx e\delta_0$. Although it was not explicitly mentioned in the work by Levich (1962), $We_{S,\max}$ can be re-written as $We_{S,\max} = 3Re_d \tau_w D / \kappa^2 \sigma$, which is essentially the Weber number based on the wall shear stress ($We_\tau = \tau_w D / \sigma$) multiplied by the droplet Reynolds number $Re_c = U_\tau D / \nu_c$ based on U_τ and the carrier-phase fluid properties.

Yi et al. (2021) studied the behavior of an oil-water emulsion in a Taylor-Couette (TC) system, which consists of a fluid layer between two counter-rotating cylinders. The resulting flows featured two thin turbulent boundary layers (TBLs) near the surfaces of the inner and outer cylinders, leaving a larger bulk region with more homogeneous and isotropic turbulence. Yi et al. (2021) first employed the KH framework, assuming that most of the droplet breakup occurred within the bulk region. Although the scaling law was verified, as the results were reanalyzed (Yi et al. 2022, 2023), it became evident that the value of the critical Weber number is much smaller than 1, from 0.013 to 0.018 using the bulk turbulence, implying that the turbulent stresses were not sufficient to overcome the interfacial tension in the bulk. This led them to conclude that the majority of droplets stayed in the bulk but most breakup occurred in the TBLs. When using Levich's definition of Weber number, Yi et al. (2022) found that the critical Weber number is close to 5, which is order unity and more reasonable. This finding suggests that the breakup was indeed driven primarily by the mean shear in the TBL, whose thickness was around 5 times the average droplet diameter.

Bubble breakup also occurs when they are directly injected into the near-wall region of a TBL. Madavan et al. (1985) found that the bubble size in the TBL is determined by the free-stream velocity and gas flow rate, and is not affected by the method of gas injection. This finding implies that the size distribution of bubbles is primarily controlled by breakup and coalescence. Rather than following equation 3, Pal et al. (1988) proposed a new way to calculate the Weber number by estimating the local energy dissipation rate $\epsilon \sim U_\tau^3/\theta$ (θ is the momentum thickness) experienced by bubbles based on the turbulence within the boundary layer. Sanders et al. (2006) revised this definition, replacing the momentum thickness θ with κy , resulting in a new definition of the turbulent Weber number.

$$We_t = \frac{2\rho_c U_\tau^2 D^{5/3}}{(\kappa y)^{2/3} \sigma} \quad 4.$$

Bubbles located approximately $y = 1$ mm ($y \approx 370\delta_0$) away from the wall in flows with a friction velocity of $U_\tau = 0.37$ m/s have been observed to have a size distribution of 320 ± 130 μm (Sanders et al. 2006). This size distribution can be explained by assuming We_t in equation 4 has a critical value. But it is important to note that, for a critical We_t near unity, We_S using equation 3 is roughly 19.

2.1.3. Mixed regime ($We_t \approx We_s$). Most turbulent flows, e.g. homogeneous shear flow (Rosti et al. 2019, Trefftz-Posada et al. 2023), turbulent pipe or channel flows (Angeli & Hewitt 2000, Scarbolo et al. 2015, Mangani et al. 2022), breaking waves (Garrett et al. 2000, Deane & Stokes 2002), turbulent jets (Martínez-Bazán et al. 1999), von Kármán swirling flow (Ravichandar et al. 2022), or stirred tanks (Shinnar 1961), typically involve both large-scale flows and turbulence.

Efforts have been made to minimize the impact of large-scale flows by injecting bubbles or droplets in regions that are closer to HIT, such as the centerline of jets (Martínez-Bazán et al. 1999) or the center of the von Kármán swirling flow (Ravichandar et al. 2022). However, as the injected bubbles or droplets are carried away from the injection point, the influence of large-scale flows may still be present.

In chemical or petroleum engineering, the size of oil droplets broken by turbulence in pipes or stirred tanks is often studied using the critical Weber number defined based on the global energy dissipation rate $\langle \epsilon \rangle$, where $\langle \dots \rangle$ represents the ensemble average over the entire device. For batch rotor-stator systems and conventional stirred tanks, $\langle \epsilon \rangle$ scales with the rotor speed N and the rotor diameter L , as expressed by $\langle \epsilon \rangle \sim N^3 L^2$ (Rushton 1950, Chen & Middleman 1967). This $\langle \epsilon \rangle$ leads to the critical Weber number being defined as $We_t^c = \rho_c N^2 L^{4/3} D^{5/3} / \sigma$, from which the critical drop size can then be determined.

In pipe flows, the global energy dissipation rate is expressed as $\langle \epsilon \rangle = f U_c^3 / 2 D_p$, where f is the friction factor, U_c is the mean axial velocity of the continuous phase, and D_p is the pipe diameter. This leads to a critical Weber number that scales with $D f^{2/3}$. However, Kubie & Gardner (1977) argued that the velocity scale should be the fluctuation velocity, not the centerline velocity. The fluctuation velocity is approximately equal to $1.3 U_\tau$, where $U_\tau = (f/8)^{1/2} U_c$. Based on this, the critical Weber number can be rewritten as $We_t^c = f \rho_c D U_c^2 / \sigma$, which scales with f instead of $f^{2/3}$. However, experiments conducted by Angeli & Hewitt (2000) found that the critical drop size scales with f^{-3} , albeit from a very narrow range of f . Thus, more experiments are needed to fully resolve the debate and determine the appropriate relationship between the critical drop size and friction factor in pipe flows.

2.1.4. Viscous effects in the inertia-dominated regime. For droplets with size $D \gg \eta$, the deformation is dominated by flow inertia and the viscosity of the carrier phase can be neglected. However, the inner viscous damping may still play a significant role in deformation dynamics, comparable or even exceeding the impact of surface tension, as quantified by the dimensionless number, Oh .

Davies (1985) and Calabrese et al. (1986) considered this problem and assumed a total balance of stresses between the external forcing by turbulence and internal damping: $\rho_c (\epsilon D)^{2/3} \sim \sigma / D + \mu_d (\epsilon D)^{1/3} \sqrt{\rho_c / \rho_d} / D$. It can also be expressed in the dimensionless form, $We_t \sim c_1 + c_2 Oh^2 Re_d \sqrt{\rho_c / \rho_d}$, where $Re_d = \rho_d (\epsilon D)^{1/3} D / \mu_d$ is the droplet Reynolds number based on the eddy velocity and inner fluid properties, and c_1 and c_2 are two fitting constants. Droplets will deform if the left side is larger than the right side, which implies that quantities of interest \mathcal{Q} (e.g. aspect ratio or breakup frequency) should be a function of the new dimensionless number following

$$\mathcal{Q} = f \left(\frac{We_t}{c_1 + c_2 Oh^2 Re_d \sqrt{\rho_c / \rho_d}} \right) \quad 5.$$

Equation 5 indicates that, for deformation and breakup, the primary dimensionless number is We_t when the inner viscous damping is negligible, and $We_t / Oh^2 Re_d \sqrt{\rho_c / \rho_d}$ when it is

important to consider.

To investigate the viscous effect, Eastwood et al. (2004) injected oil droplets in a turbulent jet along the centerline, using the same setup as Martínez-Bazán et al. (1999) in their investigation of bubble breakup. The values of Oh in the experiment ranged from $\mathcal{O}(10^{-2})$ to $\mathcal{O}(10^{-1})$, and We_t was roughly $\mathcal{O}(10)$. As illustrated in **figure 1b**, the experiment revealed a clear long filament, indicating a significant deformation preceding breakup. The extent of stretching increased with an increase in droplet viscosity, and droplets within the inertial sub-range stretched to lengths comparable to the local integral scale before fragmentation. This long filament was confirmed by other experiments (Andersson & Andersson 2006, Solsvik & Jakobsen 2015) and simulations (Håkansson et al. 2022), and it was found to be connected to the large number of daughter droplets generated from droplet breakup.

Recognizing the importance of this process, Maaß & Kraume (2012) adopted the idea originally proposed by Janssen & Meijer (1993) to describe a drop elongating in one dimension and thinning in the other two exponentially over time, driven by a constant straining flow. Given a stretching rate, the breakup time could be estimated once a critical diameter of the neck was determined, which was assumed to be related to the critical Capillary number based on μ_d and the stretching rate. However, this model did not account for the instability of the filament itself (Ruth et al. 2022) or the possible interruption by small-scale eddies, as it assumed a persistent elongation at the scale of the filament.

Vankova et al. (2007) investigated the size of emulsion droplets produced using a HPH with various oils, resulting in a range of Oh from $\mathcal{O}(10^{-1})$ to $\mathcal{O}(10)$. The authors adopted equation 5 and adjusted two constants, c_1 and c_2 , to fit their experimental results. The obtained values were 0.78 and 0.37 for c_1 and c_2 respectively. However, subsequent analysis by Zhong & Ni (2023) questioned the validity of the linear combination of the restoring and dissipative terms in equation 5 and proposed a new equation to better collapse all the data.

$$\mathcal{Q} = f \left(\frac{We_t}{1 + Oh} \right) \quad 6.$$

\mathcal{Q} , in this case, is the non-dimensionalized breakup frequency. This quantity will be further discussed in detail in Section 3.2. Note that this relationship was established based on limited experimental data. In order to further examine the validity of this relationship, it is possible to use simulation databases, such as the one by Mangani et al. (2022), with well-controlled characteristics that cover a broad range of density and viscosity ratios in turbulence.

2.2. Viscous-dominated regime ($D < \eta$)

2.2.1. Experimental Methods. There are three main experimental methods for producing droplets with $D < \eta$: (a) generating turbulence with high ϵ ; the typical value of ϵ can be calculated by satisfying two criteria $Ca_t = \sqrt{\rho_c \mu_c \epsilon} D / \sigma > Ca_t^c$ and $D < (\nu_c^3 / \epsilon)^{1/4}$. (b) reducing surface tension by adding surfactants, and (c) increasing the viscosity of the carrier phase. In food processing industries, including dairy, breaking droplets into nanometer sizes is important for the desired texture, color, and stability for storage. Option (b) or (c) is less ideal due to the required food-grade chemical additives, leaving option (a) as the primary method. The HPH is the key technique for this purpose (Håkansson 2019). It uses a high-pressure piston pump (50–200 MPa) and a narrow gap ($\mathcal{O}(100)$ μm) to accelerate emulsions to velocities of up to $\mathcal{O}(100)$ m/s, creating a localized turbulent jet (Bisten & Schuchmann 2016) with ϵ in the range of $\mathcal{O}(10^8)$ to $\mathcal{O}(10^9)$ m^2/s^3 and fragmenting droplets to sizes of

$\mathcal{O}(10\text{--}100)$ nm.

The high-speed colloid mill (rotor-stator) system, is another commonly used method for emulsion preparation. This type of system is similar to the high-Reynolds-number TC system (van Gils et al. 2011, Grossmann et al. 2016), but with a small gap size ($h = \mathcal{O}(100)$ μm) and high rotor spin rate (inner cylinder with the radius of $r_i = \mathcal{O}(10)$ cm) at $\omega_i = \mathcal{O}(10^4)$ revolutions per minute (RPM), which results in a moderate Reynolds number ($Re = \omega_i r_i h / \nu_c$) at around $\mathcal{O}(10^4)$ but a significant mean shear and turbulent energy dissipation rate (Schuster et al. 2012).

2.2.2. Negligible inner viscosity $Oh \ll 1$. By systematically increasing the viscosity of the continuous oil phase (μ_c) by two orders of magnitude while keeping the dispersed aqueous phase constant (option c in the previous section), Boxall et al. (2012) studied the transition of the dynamics of droplet breakup from the inertia-dominated to the viscous-dominated regimes. The droplets were fragmented by turbulence in a customized mixing cell driven by a six-blade impeller. The droplet size was determined using the focused beam reflectance method, and the average droplet size was calculated only after the steady state was reached, which took approximately three hours.

If Oh is negligibly small, the only dimensionless number that matters to the problem is the capillary number (Ca_t). Assuming that a critical capillary number (Ca_t^c) exists, Shinnar (1961) suggested that the critical droplet size (D^c) can be determined as follows

$$D^c = \frac{Ca_t^c \sigma}{\sqrt{\mu_c \rho_c \epsilon}} \quad 7.$$

In the experiments conducted by Boxall et al. (2012), the impeller speed (N) and diameter (L) were kept almost constant, so the energy dissipation rate ($\epsilon \sim N^3 L^2$) did not vary significantly. As μ_c increased, it was shown that the droplet size remained unchanged for low values of μ_c , and scaled with $\mu_c^{-1/2}$ in the viscous-dominated regime at high μ_c . This finding provides direct support for Equation 7.

2.2.3. Large inner viscosity $Oh \gtrsim 1$. In the previous section, a water-in-oil emulsion was considered and the viscosity of the dispersed phase was negligible in comparison to the continuous phase. For other types of emulsions, such as oil-in-water, μ_d is large and the viscous damping by the inner fluid cannot be neglected, and it is likely that Ca_t^c , if it exists, is dependent on the value of Oh .

To model this dependence, Gupta et al. (2016b) proposed a model based on the physical picture of a part of the droplet, with the size of the instability length scale, being extruded from the parent droplet due to the surrounding turbulence. By assuming that the propagation timescale of the instability is dominated by the viscous diffusion of eddy momentum into the droplet, a new formulation was derived, $Ca_t^c \sim Oh^{2/5}$, indicating that the critical Capillary number is not a constant, but a function of $Oh^{2/5}$. **Figure 3a** shows the measured Ca_t^c over a range of Oh by systematically varying the types of oils used in experiments. The oil droplet size obtained from HPH was substituted into the definition of Ca_t to obtain its value. The proposed scaling seems to capture the scaling between Ca_t^c and Oh well.

This model proposed by Gupta et al. (2016b) further predicts the critical droplet size relative to all other fluid properties as follows: $D^c = C_1 (\sigma^{5/6} \mu_d^{1/3}) / [(\rho_d \sigma)^{1/5} (\mu_c \rho_c \epsilon)^{5/12}]$. Specifically, it implies that D scales with $\mu_d^{1/3}$, $\mu_c^{-5/12}$, and $\epsilon^{-5/12}$. The scaling was com-

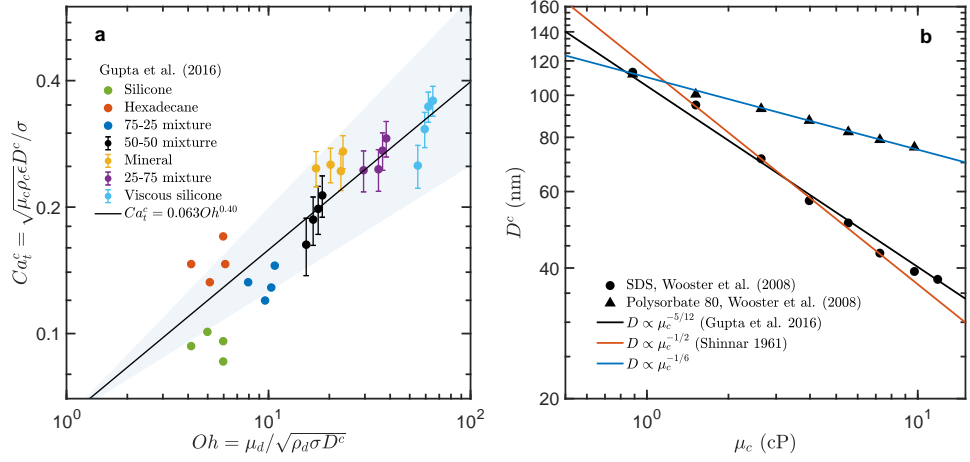


Figure 3

(a) The critical Capillary number measured from nanoemulsions made with a homogenizer as a function of Oh . The black solid line shows the $2/5$ scaling, with the blue shaded area representing the ± 0.1 uncertainty in the scaling exponent. (b) The critical drop size D^c versus the viscosity of the carrier phase for nanoemulsions made with two different types of surfactants. Figures are adapted with permission from Wooster et al. (2008) and Gupta et al. (2016a)

pared to experimental data obtained by Wooster et al. (2008), who created an oil-in-water emulsion with varying μ_c by adding various concentrations of polyethylene glycol into water. The comparison is shown in **figure 3b**. Although the proposed scaling of $D \sim \mu_c^{-5/12}$ by Gupta et al. (2016a) agrees well with the data, it is difficult to distinguish it from the one proposed by Shinnar (1961) ($D \sim \mu_c^{-1/2}$), which did not account for μ_d and Oh .

In addition, Wooster et al. (2008) actually reported two datasets using the same emulsions with the only difference being the types of surfactant added. The data adopted by Gupta et al. (2016a) is the one with 5.6 wt % sodium dodecylsulphate (SDS, 98.5%). The data using 5.6 wt % polysorbate 80 (Tween 80, 98%) is also shown in **figure 3b** (triangles), which deviates noticeably from the proposed $-5/12$ scaling, agreeing better with $D \sim \mu_c^{-1/6}$. This difference implies the possible complexity introduced by surfactant and coalescence.

Nevertheless, assuming the scaling proposed by Gupta et al. (2016a) is correct and combining the two regimes, i.e. with or without significant viscous effects, one can express quantities of interest in the problem of viscous deformation and breakup using an equation similar to equation 5

$$\mathcal{Q} = f\left(\frac{Ca_t}{c_3 + c_4 Oh^{2/5}}\right) \quad 8.$$

where c_3 and c_4 are constants that are yet to be determined to understand the critical Capillary number and the transitional Oh from the regime where the inner viscous damping is important to where it is not.

3. Deformation and breakup: timescales and dynamics

3.1. Characteristic timescales

The prediction of the evolution of the drop and bubble size distribution over space and time can be captured by solving the population balance equation, which is a Boltzmann-type equation. This approach has been widely implemented in many simulation methods to predict the dynamics of polydispersed particles, bubbles, and drops that constantly coalesce or break (Marchisio & Fox 2013, Shiea et al. 2020). In the population balance equation, there are three key quantities to describe breakup, the breakup frequency, the daughter bubble/droplet size distribution, and the number of daughters.

For breakup frequency, selecting the right timescale to non-dimensionalize it is the first challenge. The discussions of the characteristic timescale of deformation and breakup can be traced back to Section 127 of the book by Levich (1962), who considered four different breakup timescales based on the inner viscosity and interface velocity. These regimes can be determined by estimating the magnitude of the three terms, the pressure gradient $\nabla p/\rho_d$, unsteady term $\partial u_d/\partial t$, and viscous term $\nu_d \nabla^2 u_d$, in the wave equation that describes the inner fluid motion during breakup. Four timescales have been proposed, as expressed in the following equations.

$$\frac{\partial u_d}{\partial t} \sim \frac{\nabla p}{\rho_d} \sim \frac{p}{D\rho_d}; \frac{\partial u_d}{\partial t} \sim \frac{D}{\tau^2}; p \sim \frac{\sigma}{D} \Rightarrow \tau \sim \sqrt{\frac{\rho_d D^3}{\sigma}} \quad (\text{low viscosity, low speed}) \quad 9.$$

$$\frac{\nabla p}{\rho_d} \sim \nu_d \nabla^2 u_d \sim \frac{\nu_d}{D\tau}; \frac{\nabla p}{\rho_d} \sim \frac{p}{D\rho_d}; p \sim \frac{\sigma}{D} \Rightarrow \tau \sim \frac{\mu_d D}{\sigma} \quad (\text{high viscosity, low speed}) \quad 10.$$

$$\frac{\partial u_d}{\partial t} \sim \frac{\nabla p}{\rho_d} \sim \frac{p}{D\rho_d}; \frac{\partial u_d}{\partial t} \sim \frac{D}{\tau^2}; p \sim \rho_c u_c^2 \Rightarrow \tau \sim \frac{D}{u_c} \sqrt{\frac{\rho_d}{\rho_c}} \quad (\text{low viscosity, high speed}) \quad 11.$$

$$\frac{\nabla p}{\rho_d} \sim \nu_d \nabla^2 u_d \sim \frac{\nu_d}{D\tau}; \frac{\nabla p}{\rho_d} \sim \frac{p}{D\rho_d}; p \sim \rho_c u_c^2 \Rightarrow \tau \sim \frac{\mu_d}{\rho_c u_c^2} \quad (\text{high viscosity, high speed}) \quad 12.$$

where τ is the characteristic breakup timescale. u_d is the characteristic inner fluid velocity, which does not show up in the final estimation of τ because u_d scales roughly with D/τ .

The eddy turnover time has been proposed as another characteristic timescale, $t_D = \epsilon^{1/3} D^{-2/3}$, for describing bubble fragmentation in breaking waves (Garrett et al. 2000, Deane & Stokes 2002, Chan et al. 2021, Gao et al. 2021). In particular, the scaling between t_D and D directly results in the steady-state bubble size distribution scaling with $D^{-10/3}$, which was also observed in droplet breakup in turbulence (Soligo et al. 2019, Cialesi-Esposito et al. 2023a). Note that the eddy turnover time is, in fact, in line with equation 11 given by Levich (1962), if the characteristic velocity scale (u_c) of the outer flow is set as the eddy velocity at the bubble size $u_D = (\epsilon D)^{1/3}$, as proposed in the KH framework. The only difference left is that t_D does not account for the density ratio between the two phases.

Another proposed timescale is the natural oscillation frequency, f_2 , which is associated with the second eigenmode of weak-amplitude oscillations (Lamb 1879). Assuming inviscid fluids, $1/f_2 = \sqrt{(3\rho_d + 2\rho_c)D^3/30\sigma}$. Although similar to the timescale listed in equation 9, there is an important distinction to note: Levich's model only accounted for the density of the inner fluid, whereas a more complicated relationship with both ρ_d and ρ_c is required for $1/f_2$.

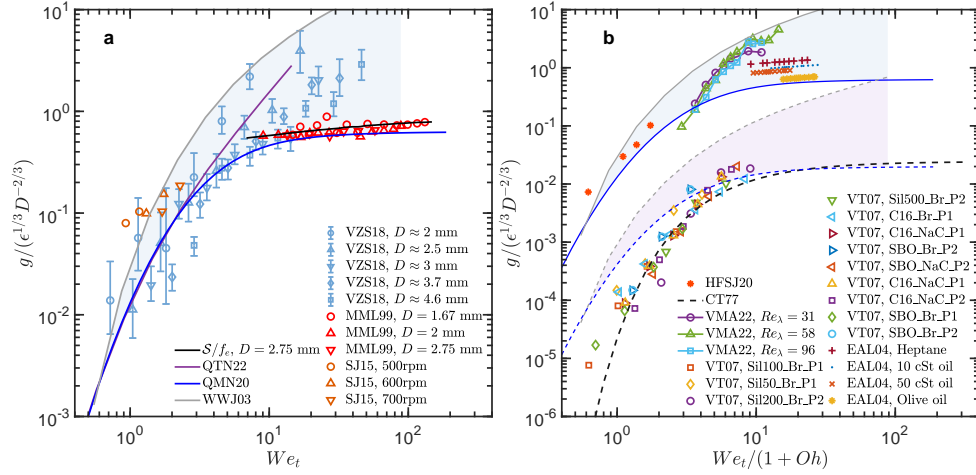


Figure 4

Breakup frequency of (a) bubbles and (b) droplets normalized by the eddy turnover frequency, $f_e = (\epsilon^{1/3} D^{-2/3})$, as a function of the key dimensionless number. The datasets that were compiled include VZS18 (Vejražka et al. 2018), MML99 (Martínez-Bazán et al. 1999), SJ15 (Solsvik & Jakobsen 2015), VT07 (Vankova et al. 2007), EAL04 (Eastwood et al. 2004), VMA22 (Vela-Martín & Avila 2022), HFSJ20 (Herø et al. 2020). Models include the ones by CT77 (Coulaloglou & Tavlarides 1977), QTN22 (Qi et al. 2022), QMN20 (Qi et al. 2020), and WWJ03 (Wang et al. 2003).

3.2. Experimental results

Zhong & Ni (2023) compiled experimental results on the breakup frequency of bubbles and oil droplets with sizes $D > \eta$ based on the recommendation made by Håkansson (2020). The eddy turnover time of size D was used as the characteristic timescale, chosen from a list of options mentioned in the previous section. **Figure 4** clearly shows that the breakup frequency drops sharply as We_t decreases, indicating droplets or bubbles with smaller We_t take longer to break. Thus, it is evident that the definition of a critical Weber number depends on the observation time (Vela-Martín & Avila 2022). If one waits longer during an experiment, smaller droplets or bubbles can be obtained for a given level of turbulence.

Although the data for bubbles (**figure 4a**) showed better agreement, discrepancies were still noticeable at high We_t . Specifically, Martínez-Bazán et al. (1999) reported a plateau in breakup frequency (g) close to 1, while Vejražka et al. (2018) claimed that g increased towards 10 without reaching a plateau. This disparity could be due to the different experimental conditions employed: the former was conducted in turbulence closer to HIT, while the latter involved injecting bubbles along the centerline of a turbulent jet. As the bubbles spread away from the centerline as they migrate downstream, they may experience mean shear.

The inverse of the mean shear rate (S) was suggested by Zhong & Ni (2023) as another potential timescale, estimated by dividing the centerline velocity of the turbulent jet by its width, following the canonical turbulent jet. The estimated shear rate is plotted as a black solid line in **figure 4a**, matching the measured breakup frequency quite well and providing an alternative timescale to consider for breakup frequency in inhomogeneous and

Breakup frequency (g): the fraction of bubbles/droplets that break per unit time in turbulence

anisotropic turbulence.

For droplet data in **figure 4b**, equation 6 mentioned in Section 2.1.4, proposed by Zhong & Ni (2023), was used to compile different datasets with different Oh . The datasets provided by Vankova et al. (2007), with Oh ranging from $\mathcal{O}(10^{-2})$ to $\mathcal{O}(10)$, collapsed with one another well using equation 6. However, when including all the datasets, a nearly two-orders-of-magnitude variation in the breakup frequency was observed. This difference primarily arises from the experiments conducted by Vankova et al. (2007) in a homogenizer, where the drop size was in the order of $\mathcal{O}(10^{-5})$ m, as compared to other experiments that involved much larger drops of $\mathcal{O}(10^{-3})$ m, implying either large systematic uncertainties between large- and small-scale experiments or a potential hidden size dependence that was not accounted for in the current selection of dimensionless groups.

The deformation and breakup of bubbles and droplets could potentially be understood under a unified framework if a suitable set of dimensionless numbers is chosen to collapse all available data. In an attempt to achieve this, Zhong & Ni (2023) selected two models that represent the upper (Wang et al. 2003) and lower (Qi et al. 2020) bounds of bubble experiments, as illustrated by the shaded area in Figure 4a. The same shaded area was overlaid twice on top of the droplet datasets in Figure 4b, once with (lower shaded area with dashed lines as bounds) and once without (upper shaded area with solid lines as bounds) the density ratio, $\sqrt{\rho_d/\rho_c}$, as suggested by Levich's timescales (Equation 11), to show how well the bubble and droplet data collapse. The inclusion of $\sqrt{\rho_d/\rho_c}$ resulted in the collapse of most of the available bubble and droplet data, except for the dataset by Vankova et al. (2007). In contrast, when the density ratio was not considered, the bubble data showed better agreement with the results by Vankova et al. (2007). This finding suggests that the existing droplet data exhibits too much disparity to draw a definitive conclusion regarding the effectiveness of including the density ratio term for characterizing the breakup timescale.

3.3. Numerical simulations

In addition to experiments, with the development of more advanced direct numerical simulation (DNS) algorithms for two-phase flows (Elghobashi 2019) and Graphics Processing Unit (GPU) based codes (Crales-Esposito et al. 2023b), it is possible to conduct a large number of simulations of breakup events to collect statistics. For example, Liu et al. (2021) implemented an efficient simulation scheme for the phase-field method to simulate the breakup of a large drop and the coalescence of $\mathcal{O}(10^3)$ drops.

In addition to the simulation schemes, in general, two strategies have been adopted so far. The first one involves a larger simulation domain with many drops and a limited number of selected dimensionless numbers, and drops are allowed to break and coalesce (Dodd & Ferrante 2016, Roccon et al. 2017, Scarbolo et al. 2015, Mangani et al. 2022, Crales-Esposito et al. 2023a). This strategy is particularly suitable for investigating breakup at high concentrations in complex environments that are relevant to many applications, such as emulsions and breaking waves. Since it simulates both breakup and coalescence in turbulence, it also helps illustrate the energy transferred between the two phases (Dodd & Ferrante 2016, Crales-Esposito et al. 2023a).

The second method relies on a smaller domain with only one drop but many more runs, ranging from hundreds (Rivière et al. 2021) to over 30,000 (Vela-Martín & Avila 2022), to cover a wider parameter space. The advantage of this method is the isolation of

the breakup events without the complication of coalescence. This approach is particularly useful for investigating parameters under which breakup takes a long time, a regime where experiments suffer from large uncertainty and finite residence time.

3.4. Deformation and breakup models

If reliable models for describing deformation and breakup can be developed, it is much more computationally efficient to integrate these models along the Lagrangian trajectories of point bubbles/droplets in turbulence to study their breakup frequency and probability. In the following, we review some of the deformation and breakup models.

For viscous fluids, Maffettone & Minale (1998) developed a model (M&M) to describe the evolution of both shape and orientation of neutrally-buoyant spheroidal droplets in a linear velocity gradient. This model was validated against several experimental studies in low Reynolds number. Recently, the model has been applied to simulating the deformation of many sub-Kolmogorov-scale neutrally-buoyant droplets ($D \ll \eta$) in turbulence by integrating the M&M equation numerically along their Lagrangian trajectories (Biferale et al. 2014, Spandan et al. 2016).

For inertia-dominated deformation and breakup, it is much more challenging to develop a deformation model. One model simplified the problem by ignoring the orientation and proposed to describe a droplet as a linear damped oscillator that is forced by the instantaneous turbulent fluctuations at the drop scale (Risso & Fabre 1998, Lalanne et al. 2019). The equation can be written in a dimensionless form as follows,

$$\frac{d^2 \hat{a}}{d\hat{t}^2} + 2\xi \frac{d\hat{a}}{d\hat{t}} + \hat{a} = K' We_t(t) \quad 13.$$

where \hat{a} represents the difference between the semi-major axis of the deformed geometry and the spherical-equivalent radius divided by $D/2$. The damping coefficient is given by $\xi = 1/2\pi\tau_d f_2$, where τ_d is the damping time scale defined as $\tau_d = D^2/80\nu_c$ for bubbles (Risso & Fabre 1998) but a much more complicated implicit solution for droplets (Lalanne et al. 2019). In contrast to previous models that assumed an additive relationship between viscous stress and surface tension (Davies 1985, Calabrese et al. 1986), this model correctly incorporated the dissipative nature of viscous damping, and it has been successfully compared to experimental data on breakup statistics, even in inhomogeneous turbulence (Galinat et al. 2007, Maniero et al. 2012).

To account for the orientation and add multiple deformation mechanisms, Masuk et al. (2021a) adapted the MnM model into the inertia-dominated regime by making three important modifications: (a) Velocity gradients were coarse-grained at the size of the bubble; (b) Deformation due to slip velocity was accounted for by using a pseudo-strain-rate tensor; and (c) A pseudo-rotation tensor was added to model the wake-induced bubble rotation. The modified model has been successfully used to predict deformation and orientation for bubbles in both turbulence and quiescent media, with the predicted statistics agreeing well with experimental data. These findings suggest that the modified model effectively captures the key mechanisms responsible for inertial deformation and breakup.

3.5. Recent models for breakup frequency

Recent advances in modeling breakup mechanisms have highlighted the importance of several previously neglected factors, including gas density, eddies of different sizes, and tur-

bulence intermittency, which we will summarize here. In the past, air bubbles were often modeled as having negligible density and viscosity. However, it has been shown that bubbles made of heavier gases can break more frequently (Wilkinson et al. 1993). This phenomenon was explained by Andersson & Andersson (2006), who pointed out that deformation typically results in a dumbbell shape with two uneven ends. As the smaller end retracts due to surface tension, air flow accelerates through the neck, which reduces the local pressure and speeds up the breakup process. Larger gas density tends to lower the local pressure and shorten the breakup time even further. These observations and proposed mechanisms have inspired new models developed by Xing et al. (2015) and Zhang et al. (2020), which incorporate the effect of backflow and gas density.

In addition to the density effect, to accurately model bubble-eddy collision, it is crucial to determine which eddy scales should be considered. The KH framework assumes that only the drop-scale eddy is significant, with both larger and smaller scales being negligible. Conversely, some models consider eddies of all length scales from the turbulent spectrum (Karimi & Andersson 2018, Castellano et al. 2019). However, recent research by Vela-Martín & Avila (2021), which employed direct numerical simulation of a single drop being deformed in turbulence, found that the impact of eddies with different length scales on the variation of surface free energy is not equal. Turbulent fluctuations at scales smaller than the drop diameter cause the majority of surface deformation, while the contribution of scales close to or larger than D is relatively minor.

Qi et al. (2022) designed an experiment using the head-on collision between two vortex rings to isolate the turbulent scales. During the early stage before the collision, only intact large-scale vortices were accessible, while the post-collision late stage was filled with many small eddies. Despite a lower overall We_t in the late stage, bubbles were found to break up in a more violent and faster manner due to the presence of small eddies. Building on this finding, the authors developed a new model that considers not only the stress criterion, which requires the incoming eddy to exert sufficient stress to overcome the restoring surface tension, but also the time scale. The breakup must occur within the time before the bubble relaxes. This key idea emphasizes that, instead of being gradually and consistently stretched by flows at their own length scales, bubbles are fragmented by small eddies, resulting in a sudden and intense local deformation over a short period of time. The predicted breakup frequency as a function of We_t is shown as the purple solid line in **figure 4a**, which agrees with the experimental data by Vejražka et al. (2018).

Numerous studies have investigated the effect of turbulence intermittency on bubble breakup. Recent models have examined the impact of intermittency on the turbulent energy spectrum, as noted by Bagkeris et al. (2021) and Solsvik & Jakobsen (2016). However, the effect of intermittency on the distribution of ϵ , which can be derived from the multi-fractal model and described by a log-normal distribution (Meneveau & Sreenivasan 1991), is more pronounced than that on the energy spectrum. This distribution can be incorporated into modeling quantities such as the breakup probability (Masuk et al. 2021c), eddy velocity (Qi et al. 2022), and breakup frequency (Qi et al. 2020).

In particular, Qi et al. (2020) modified the model originally proposed by Martínez-Bazán et al. (1999) to account for the non-negligible breakup frequencies for small bubbles when exposed to intermittent turbulent eddies. The model prediction is shown as the blue solid line in **figure 4a** and the lower bounds for the two shaded areas in **figure 4b**. The classical model by Coualoglou & Tavlarides (1977) (black dashed line) fits the data by Vankova et al. (2007) well. However, for most other datasets, a slower decay of the breakup frequency g

as We_t decreases is observed, which is better predicted by Qi et al. (2020).

4. Modulation of mass, momentum, and heat transfer by deformation

4.1. Deformation affecting effective bubble forces

The motion of large bubbles and droplets in turbulence can be characterized by the combined effect of multiple hydrodynamic forces, such as buoyancy, drag, lift, added mass, Basset history, and pressure forces (Magnaudet & Eames 2000, Sridhar & Katz 1995). As the majority of these forces are shape-dependent, it is not surprising that bubble and droplet deformability can significantly impact their translational motion and local concentration in turbulence.

Most research on forces experienced by bubbles has focused on their behavior in laminar shear (Legendre & Magnaudet 1998, Tomiyama et al. 2002, Lu & Tryggvason 2008, Dijkhuizen et al. 2010, Hessekemper et al. 2020). Bubble deformation, driven primarily by buoyancy, is measured by Eo . As Eo increases, the lift force undergoes a transition from positive to negative values. This shift in direction is attributed to the stretching and tilting of vorticity generated at the bubble surface, which transforms into a pair of counter-rotating streamwise vortices in the bubble wake. These vortices have the opposite sign compared to those produced around a spherical bubble, resulting in a negative lift force. In addition to vorticity production, direct asymmetric deformation caused by external shear can also lead to negative lift (Zhang et al. 2021, Hidman et al. 2022).

In turbulence, Sugrue (2017) proposed a new dimensionless number taking the product of Eo and the ratio between the local turbulent kinetic energy and the squared relative velocity between the two phases. This new number is linked to the Weber number based on the fluctuation velocity. The authors carried out extensive simulations, varying lift coefficients, and minimizing the differences between experimental and simulated results. This allowed them to extract lift coefficients for different flow conditions. The results showed that the lift coefficients exhibited a similar inversion to those observed in laminar shear flow. However, two key differences were noted. Firstly, the magnitude of the coefficients was much smaller, and secondly, the inversion diameter was smaller for turbulence-driven cases.

To measure the lift coefficient in turbulence, Salibindla et al. (2020) conducted an experiment in nearly HIT. Although the flow does not have a mean shear, the bubbles were constantly subjected to local shear and vorticity. The transition of bubble rising velocity in turbulence from lower to faster than its counterpart in an otherwise-quiescent medium was found as the bubble size increased. Based on this finding and the access to the statistics of both phases, the lift and drag forces experienced by bubbles with different sizes were determined, and the lift inversion at smaller bubble size was observed experimentally. The lift inversion was correlated to the turbulence-induced deformation measured by We_t , which is close to 1 as the inversion occurs, suggesting that turbulence-induced bubble deformation becomes essential. The transition of the bubble's rising velocity was linked to the preferential sampling of different regions (upward or downward) in turbulence. This work also supports the mechanism proposed by Spelt & Biesheuvel (1997) that small spherical bubbles tend to preferentially sample the downward flows in turbulence instead of being trapped in the vortex cores (Wang & Maxey 1993) and also quantitatively explains other previous experiments (Poorte & Biesheuvel 2002, Aliseda & Lasheras 2011, Prakash et al. 2012).

It is worth noting that the transition of bubble rising velocity was not observed in an-

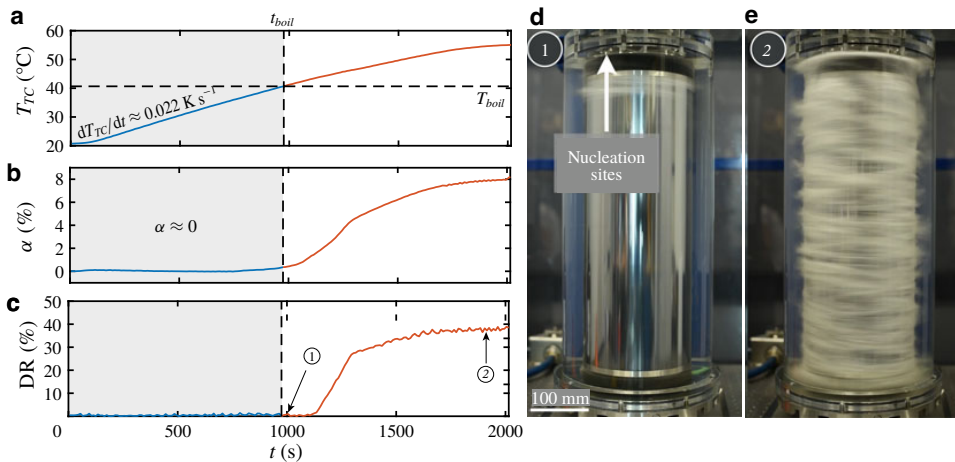


Figure 5

The drag of turbulent Taylor–Couette flow during its transition from non-boiling (grey shaded areas) to boiling at $t = t_{boil}$ and the key quantities, including (a) Liquid temperature T_{TC} , (b) volume fraction α , (c) drag reduction (DR) as a function of time; Two time steps correspond to the photographs shown in (d) and (e). Figures are adapted with permission from Ezeta et al. (2019).

other work conducted by Ruth et al. (2021). In this study, the change in rise velocity was attributed mainly to drag rather than lift, highlighting the need for further investigation into how deformable bubbles modify lift and drag forces in intense turbulence where deformation is driven by local turbulence instead of buoyancy. Nevertheless, once lift and drag forces are determined, the added mass force can also be evaluated experimentally. Recent work by Salibindla et al. (2021) showed that the added mass force experienced by bubbles in turbulence can be accurately modeled using the solid spheroid approximations (Lamb 1879). These findings suggest that the instantaneous added-mass force experienced by deformable bubbles can be approximated by appropriately oriented spheroids with the correct instantaneous aspect ratios.

4.2. Turbulent drag reduction

The deformation and breakup of bubbles and drops in turbulent boundary layers have been extensively studied in the context of drag reduction (Ceccio 2010, Murai 2014) in various configurations, including turbulent TC (van Gils et al. 2013), flat plates (Sanders et al. 2006), channel flows (Murai et al. 2007, Tanaka et al. 2021), and even under the model ship hull (Tanaka et al. 2022). Several mechanisms have been proposed to explain the origin of the bubble-induced drag reduction effect (Ferrante & Elghobashi 2004, Lu et al. 2005, Lu & Tryggvason 2008, van den Berg et al. 2007). The successful drag reduction experiments have been summarized by Murai (2014) in two regimes: relatively small bubbles in high-speed flows or large bubbles in low-speed flows. A recent overview of this topic was presented by Lohse (2018), who highlights the difference between bubble-induced drag reduction at small Reynolds numbers and large Reynolds numbers, attributed to the effects of Froude number and Weber number, respectively.

While most experiments on bubble-mediated drag reduction focused on large-scale aver-

aged skin friction, a few studies measured the couplings between the two phases. Kitagawa et al. (2005) conducted 2D simultaneous measurements of both phases in a horizontal turbulent channel to determine the mechanism of drag reduction caused by bubbles. The bubbles, which were roughly $530 \mu\text{m}$ and deformable close to the wall, were shown to cause a drop in the Reynolds stress of the carrier phase. The reduction ratio was almost the same as that of the skin friction coefficient. Murai et al. (2007) measured the fluctuation of the wall shear stress due to the passage of individual deformable bubbles with size comparable to the boundary layer thickness using a shear transducer. They found that the bubbles considerably reduced the local wall shear stress, which was induced by the two roll vortices upstream and downstream of the bubble that modified the local turbulent shear stress (Oishi & Murai 2014).

Drag reduction has been a topic of extensive study in the context of high-Reynolds-number TC systems because it is a closed system where frictional drag can be measured as the global torque. van Gils et al. (2013) showed that the system transitions from moderate drag reduction of 7% to a more significant one with nearly 40% drag reduction at Reynolds number (Re) above 10^6 and gas void fraction of 4%. This transition was observed as the Weber number crosses one and the bubble becomes more deformable, even as the size becomes smaller as Re increases. As Re increases and drag decreases, a larger bubble aspect ratio was observed (as shown in **figure 1a**), signaling the connection between deformation and drag reduction. This point was further supported by Verschoof et al. (2016), who showed that the large drag reduction (40%) could be ‘turned off’ by adding some surfactant. The surfactant reduces surface tension and hinders coalescence, which leads to much smaller bubbles with smaller We_t . Similar levels of drag reduction were also observed in boiling TC driven by vapor bubbles, again due to their deformation in turbulence, as shown in **figure 5**. As the vapor bubble volume fraction α increases, the probability of finding a larger value of We_t increases, probably due to the presence of more-deformable larger bubbles formed by coalescence. Finally, a recent study by Wang et al. (2022) investigated how viscosity ratios between the two phases affect drag in TC and found that the drag coefficient increases as the inner viscosity increases and drop deformability weakens, further reaffirming the importance of deformation in turbulent drag reduction.

Extensive simulations have been also conducted to explore the potential mechanism of drag reduction driven by deformable bubbles/droplets. Iwasaki et al. (2001) demonstrated that the droplets can attenuate near-wall streamwise vortices via deformation. Lu et al. (2005) found that large deformable bubbles can lead to significant drag reduction by suppressing streamwise vorticity near the wall, whereas less-deformed bubbles tend to bring additional shear rate near the viscous sublayer to increase drag. Spandan et al. (2018) reported that deformable bubbles can reduce drag in TC flows by modulating dissipation in their wakes, regardless of whether the carrier fluid is weakly or highly turbulent. Overall, these studies underscore different mechanisms at play in bubble/droplet-mediated turbulent drag reduction through a deformable interface.

4.3. Turbulence modulation

Dodd & Ferrante (2016) performed direct numerical simulations to investigate the behavior of finite-sized drops in decaying isotropic turbulence, exploring a range of Weber numbers, density ratios, and viscosity ratios between the two phases. In this work, the turbulence kinetic energy (TKE) equations were derived to capture the energy transfer between two

phases, with a particular focus on the role of interfacial energy. It was shown that, while the presence of droplets always enhances the dissipation rate near the droplet interface, the initial turbulence decay rate is faster in the presence of more deformable drops (i.e., larger Weber numbers). However, the decay rate becomes independent of the Weber number later on, likely because the turbulence has decayed to a point where it is no longer strong enough to deform or break any drops. The study also demonstrated that droplet coalescence acts as a source of TKE through the power of surface tension, while breakup serves as a sink of TKE.

In their investigation of turbulence modulation at different scales, Freund & Ferrante (2019) analyzed the same data generated by Dodd & Ferrante (2016) using wavelet transforms instead of Fourier transforms because wavelet restricts the effects of non-smoothness locally while preserving spatial information. At a distance larger than 5η or $D/4$, the carrier-phase spectra remained nearly unaffected, but the energy at high wavenumbers increased close to the drop interface due to enhanced local velocity gradients. They also observed that drops with larger density ratios reduced the energy at low wavenumbers compared to neutrally-buoyant drops. In a separate study, Scarbolo et al. (2013) examined the interaction between turbulence and one large deformable droplet and showed that the presence of the interface results in vorticity generation and turbulence damping near the interface, and the distance from the interface where these effects are present depends on the surface tension.

The spectrum analysis of turbulence modulation by drops in HIT was also studied by Mukherjee et al. (2019). They showed that the presence of dispersed drops leads to a transfer of energy from large scales to small scales, as the drops subtract energy from the former and inject it into the latter. This transfer of energy is reflected in the energy spectra, which cross the spectra of the single-phase turbulence at a length scale close to the Kolmogorov-Hinze scale, as initially proposed by Perlekar et al. (2014) for a different system. Crialesi-Esposito et al. (2022) provided further insights into the mechanisms behind this phenomenon, showing that surface tension forces play a key role in absorbing energy from large scales and reducing its transfer through advection terms. Eventually, this energy is transferred to small scales by surface tension. They also noted that the modulation of turbulence spectra is more sensitive to the viscosity ratio, while the scale-by-scale energy budget depends more on the volume fractions.

Bubble-induced turbulence in a swarm of rising bubbles in an otherwise quiescent fluid has been extensively studied in recent years. The phenomenon has been investigated (Riboux et al. 2010, Innocenti et al. 2021, Pandey et al. 2022), modelled (Ma et al. 2017, Du Cluzeau et al. 2019), and also recently reviewed by Risso (2018) and Mathai et al. (2020). Mercado et al. (2010) measured the energy spectrum of the carrier phase using a phase-sensitive anemometry and found that the energy decays with wave number following a power law of -3.2 , which is close to the -3 scaling proposed by Lance & Bataille (1991). They also observed that even at a small gas volume fraction, typically from 0.28% to 0.74%, deformable bubbles tend to cluster along the vertical direction at both small and large scales, which was attributed to deformation (Bunner & Tryggvason 2003).

4.4. Heat and mass transfer

The study of heat and mass transfer in turbulent multiphase flows is a complex and multifaceted topic that deserves a dedicated review because a wide range of relevant inter-

facial transfer phenomena, including boiling/condensation (Russo et al. 2014), dissolution (Mac Huang et al. 2015, Farsoiya et al. 2023), melting (Machicoane et al. 2013), evaporation (Birouk & Gökalp 2006, Duret et al. 2012, Marié et al. 2014, Méès et al. 2020), and the induced Stefan flow, can be potentially modulated by turbulence and a deformable interface.

Deformation and breakup have been shown to affect heat and mass transfer. However, the extent of their influence on these processes is not yet fully understood beyond their effect on the size distribution and interfacial area. Recently, Albernaz et al. (2017) investigated the deformation and heat transfer of a single drop in HIT and found a negative correlation between local curvature and temperature on the droplet surface. Wang et al. (2019) found that the kinematics of deformable bubbles and droplets could significantly enhance the heat transfer in turbulent convection, and revealed that the emergent size distribution of the bubbles and droplets in the system governed the degree of heat transfer enhancement achievable. Dodd et al. (2021) used direct numerical simulation (DNS) to study finite-size, deformable, and evaporating droplets in HIT, and they showed that higher surface curvature induced by deformation and breakup leads to higher evaporation rates, especially for cases with large Weber numbers. Shao et al. (2022) demonstrated that the Stefan flow induced by evaporation reduces the coalescence rate and attenuates the turbulence kinetic energy. Scapin et al. (2022) extended the problem to homogeneous shear flow and found that the larger surface area due to deformation leads to an overall larger mass transfer rate for drops with higher Weber numbers in persistent mean shear. They also observed a weak correlation between the interfacial mass flux and curvature at high temperature and a positive correlation at large Weber number, low ambient temperature, and slower evaporation. Boyd & Ling (2023) simulated the aerodynamic breakup of an acetone drop in a high-speed and high-temperature vapor stream and showed that as the drop deforms, the increase of frontal surface area results in a significantly increased rate of evaporation and a nonlinear decrease in drop volume over time.

SUMMARY POINTS

1. New experiments capable of measuring the shape of deforming bubbles and drops simultaneously with the detailed surrounding turbulence in 3D have been made possible with the advancement of diagnostic methods and new facilities that can generate controlled turbulence.
2. Turbulence in many applications is usually inhomogeneous and anisotropic. Deformation and breakup in these systems are often subjected to both a non-uniform distribution of turbulence intensity and a persistent large-scale shear.
3. The primary dimensionless parameter for breakup driven by the flow inertia of the carrier phase ($D \gg \eta$) is $We/(1 + Oh)$, while for breakup driven by the viscous stress of the carrier phase ($D \ll \eta$), it is $Ca/(c_3 + c_4 Oh^{2/5})$. These relationships were established based on limited data, and further studies are required to validate them.
4. Deformation is driven by large-scale eddies and breakup is accelerated by small-scale eddies. The multiscale nature of breakup is a key component in understanding the inertia-dominated breakup.
5. Existing works showed the intricacies of the interplay between the local interface curvature, local interfacial mass flux, and the induced Stefan flow for two-phase heat and mass transfer with a deformable interface.

FUTURE ISSUES

1. Understanding the potential synergies between large-scale shear and local turbulence in deforming and breaking bubbles/droplets requires additional research.
2. The impact of density ratio, Reynolds number, and additives such as salt and surfactant on deformation and breakup should be further investigated, as their roles remain poorly understood despite previous research.
3. Additional research is needed to better understand how the time history of bubbles or droplets affects their deformation and breakup processes as they traverse through inhomogeneous turbulence with varying local intensities.

DISCLOSURE STATEMENT

The author is not aware of any affiliations, memberships, funding, or financial holdings that might be perceived as affecting the objectivity of this review.

ACKNOWLEDGMENTS

The author thanks colleagues who provided advice and suggestions on the manuscript. The author also acknowledges support from NSF grant CBET 1854475 and CAREER-1905103 and Office of Naval Research grant N00014-21-1-2083 and N00014-21-1-2123.

LITERATURE CITED

- Albernaz DL, Do-Quang M, Hermanson JC, Amberg G. 2017. Droplet deformation and heat transfer in isotropic turbulence. *J. Fluid Mech.* 820:61–85
- Aliseda A, Lasheras J. 2011. Preferential concentration and rise velocity reduction of bubbles immersed in a homogeneous and isotropic turbulent flow. *Phys. Fluids* 23(9):093301
- Andersson R, Andersson B. 2006. On the breakup of fluid particles in turbulent flows. *AIChE J.* 52(6):2020–2030
- Angeli P, Hewitt GF. 2000. Drop size distributions in horizontal oil-water dispersed flows. *Chem. Eng. Sci.* 55(16):3133–3143
- Bagkeris I, Michael V, Prosser R, Kowalski A. 2021. Modeling drop breakage using the full energy spectrum and a specific realization of turbulence anisotropy. *AIChE J.* 67(7):e17201
- Bakhuis D, Ezeta R, Bullee PA, Marin A, Lohse D, et al. 2021. Catastrophic phase inversion in high-Reynolds-number turbulent Taylor-Couette flow. *Phys. Rev. Lett.* 126(6):064501
- Balachandar S, Eaton JK. 2010. Turbulent dispersed multiphase flow. *Annu. Rev. Fluid Mech.* 42:111–133
- Bellani G, Variano EA. 2012. Slip velocity of large neutrally buoyant particles in turbulent flows. *New J. Phys.* 14(12):125009
- Biferale L, Meneveau C, Verzicco R. 2014. Deformation statistics of sub-Kolmogorov-scale ellipsoidal neutrally buoyant drops in isotropic turbulence. *J. Fluid Mech.* 754:184–207
- Birouk M, Gökalp I. 2006. Current status of droplet evaporation in turbulent flows. *Prog. Energy Combust. Sci.* 32(4):408–423

- Bisten A, Schuchmann HP. 2016. Optical measuring methods for the investigation of high-pressure homogenisation. *Processes* 4(4):41
- Boxall JA, Koh CA, Sloan ED, Sum AK, Wu DT. 2012. Droplet size scaling of water-in-oil emulsions under turbulent flow. *Langmuir* 28(1):104–110
- Boyd B, Ling Y. 2023. A consistent volume-of-fluid approach for direct numerical simulation of the aerodynamic breakup of a vaporizing drop. *Comput. Fluids* 254:105807
- Brandt L, Coletti F. 2022. Particle-laden turbulence: progress and perspectives. *Annu. Rev. Fluid Mech.* 54:159–189
- Bunner B, Tryggvason G. 2003. Effect of bubble deformation on the properties of bubbly flows. *J. Fluid Mech.* 495:77–118
- Calabrese RV, Chang T, Dang P. 1986. Drop breakup in turbulent stirred-tank contactors. part i: Effect of dispersed-phase viscosity. *AIChE J.* 32(4):657–666
- Castellano S, Carrillo L, Sheibat-Othman N, Marchisio D, Buffo A, Charton S. 2019. Using the full turbulence spectrum for describing droplet coalescence and breakage in industrial liquid-liquid systems: Experiments and modeling. *Chem. Eng. J.* 374:1420–1432
- Ceccio SL. 2010. Friction drag reduction of external flows with bubble and gas injection. *Annu. Rev. Fluid Mech.* 42:183–203
- Chan WHR, Johnson PL, Moin P, Urzay J. 2021. The turbulent bubble break-up cascade. part 2. numerical simulations of breaking waves. *J. Fluid Mech.* 912:A43
- Chen HT, Middleman S. 1967. Drop size distribution in agitated liquid-liquid systems. *AIChE J.* 13(5):989–995
- Coulaloglou C, Tavlarides LL. 1977. Description of interaction processes in agitated liquid-liquid dispersions. *Chem. Eng. Sci.* 32(11):1289–1297
- Crialesi-Esposito M, Chibbaro S, Brandt L. 2023a. The interaction of droplet dynamics and turbulence cascade. *Commun. Phys.* 6(1):5
- Crialesi-Esposito M, Rosti ME, Chibbaro S, Brandt L. 2022. Modulation of homogeneous and isotropic turbulence in emulsions. *J. Fluid Mech.* 940:A19
- Crialesi-Esposito M, Scapin N, Demou AD, Rosti ME, Costa P, et al. 2023b. FluTAS: A GPU-accelerated finite difference code for multiphase flows. *Comput. Phys. Commun.* 284:108602
- Davies J. 1985. Drop sizes of emulsions related to turbulent energy dissipation rates. *Chem. Eng. Sci.* 40(5):839–842
- Deane G, Stokes M. 2002. Scale dependence of bubble creation mechanisms in breaking waves. *Nature* 418(6900):839
- Dijkhuizen W, van Sint Annaland M, Kuipers J. 2010. Numerical and experimental investigation of the lift force on single bubbles. *Chem. Eng. Sci.* 65(3):1274–1287
- Dodd MS, Ferrante A. 2016. On the interaction of Taylor length scale size droplets and isotropic turbulence. *J. Fluid Mech.* 806:356–412
- Dodd MS, Mohaddes D, Ferrante A, Ihme M. 2021. Analysis of droplet evaporation in isotropic turbulence through droplet-resolved dns. *Int. J. Heat Mass Transf.* 172:121157
- Du Cluzeau A, Bois G, Toutant A. 2019. Analysis and modelling of Reynolds stresses in turbulent bubbly up-flows from direct numerical simulations. *J. Fluid Mech.* 866:132–168
- Duret B, Luret G, Reveillon J, Ménard T, Berlemont A, Demoulin FX. 2012. DNS analysis of turbulent mixing in two-phase flows. *Int. J. Multiph. Flow* 40:93–105
- Eastwood CD, Armi L, Lasheras J. 2004. The breakup of immiscible fluids in turbulent flows. *J. Fluid Mech.* 502:309–333
- Elghobashi S. 2019. Direct numerical simulation of turbulent flows laden with droplets or bubbles. *Annu. Rev. Fluid Mech.* 51:217–244
- Ezeta R, Bakhuis D, Huisman SG, Sun C, Lohse D. 2019. Drag reduction in boiling Taylor–Couette turbulence. *J. Fluid Mech.* 881:104–118
- Farsoiya PK, Magdelaine Q, Antkowiak A, Popinet S, Deike L. 2023. Direct numerical simulations of bubble-mediated gas transfer and dissolution in quiescent and turbulent flows. *J. Fluid Mech.*

- 954:A29
- Ferrante A, Elghobashi S. 2004. On the physical mechanisms of drag reduction in a spatially developing turbulent boundary layer laden with microbubbles. *J. Fluid Mech.* 503:345–355
- Freund A, Ferrante A. 2019. Wavelet-spectral analysis of droplet-laden isotropic turbulence. *J. Fluid Mech.* 875:914–928
- Galinat S, Risso F, Masbernat O, Guiraud P. 2007. Dynamics of drop breakup in inhomogeneous turbulence at various volume fractions. *J. Fluid Mech.* 578:85–94
- Gao Q, Deane GB, Shen L. 2021. Bubble production by air filament and cavity breakup in plunging breaking wave crests. *J. Fluid Mech.* 929:A44
- Garrett C, Li M, Farmer D. 2000. The connection between bubble size spectra and energy dissipation rates in the upper ocean. *J. Phys. Oceanogr.* 30(9):2163–2171
- Grossmann S, Lohse D, Sun C. 2016. High-Reynolds number Taylor-Couette turbulence. *Annu. Rev. Fluid Mech.* 48:53–80
- Gupta A, Eral HB, Hatton TA, Doyle PS. 2016a. Controlling and predicting droplet size of nanoemulsions: scaling relations with experimental validation. *Soft Matter* 12(5):1452–1458
- Gupta A, Eral HB, Hatton TA, Doyle PS. 2016b. Nanoemulsions: formation, properties and applications. *Soft Matter* 12(11):2826–2841
- Håkansson A. 2019. Emulsion formation by homogenization: Current understanding and future perspectives. *Annu. Rev. Food Sci. Technol.* 10:239–258
- Håkansson A. 2020. On the validity of different methods to estimate breakup frequency from single drop experiments. *Chem. Eng. Sci.* 227:115908
- Håkansson A, Crialesi-Esposito M, Nilsson L, Brandt L. 2022. A criterion for when an emulsion drop undergoing turbulent deformation has reached a critically deformed state. *Colloids Surf. A: Physicochem. Eng. Asp.* 648:129213
- Herø EH, La Forgia N, Solsvik J, Jakobsen HA. 2020. Single drop breakage in turbulent flow: Statistical data analysis. *Chem. Eng. Sci.: X* 8:100082
- Hessenkemper H, Ziegenhein T, Lucas D. 2020. Contamination effects on the lift force of ellipsoidal air bubbles rising in saline water solutions. *Chem. Eng. J.* 386:121589
- Hidman N, Ström H, Sasic S, Sardina G. 2022. The lift force on deformable and freely moving bubbles in linear shear flows. *J. Fluid Mech.* 952:A34
- Hinze J. 1955. Fundamentals of the hydrodynamic mechanism of splitting in dispersion processes. *AIChE J.* 1(3):289–295
- Homann H, Bec J. 2010. Finite-size effects in the dynamics of neutrally buoyant particles in turbulent flow. *J. Fluid Mech.* 651:81–91
- Innocenti A, Jaccod A, Popinet S, Chibbaro S. 2021. Direct numerical simulation of bubble-induced turbulence. *J. Fluid Mech.* 918:A23
- Iwasaki T, Nishimura K, Tanaka M, Hagiwara Y. 2001. Direct numerical simulation of turbulent couette flow with immiscible droplets. *Int. J. Heat Fluid Flow* 22(3):332–342
- Janssen J, Meijer H. 1993. Droplet breakup mechanisms: Stepwise equilibrium versus transient dispersion. *J. Rheol.* 37(4):597–608
- Karimi M, Andersson R. 2018. An exploratory study on fluid particles breakup rate models for the entire spectrum of turbulent energy. *Chem. Eng. Sci.* 192:850–863
- Kitagawa A, Hishida K, Kodama Y. 2005. Flow structure of microbubble-laden turbulent channel flow measured by piv combined with the shadow image technique. *Exp. Fluids* 38(4):466–475
- Kolmogorov A. 1949. On the breakage of drops in a turbulent flow, In *Dokl. Akad. Nauk. SSSR*, vol. 66, pp. 825–828
- Kolmogorov AN. 1962. A refinement of previous hypotheses concerning the local structure of turbulence in a viscous incompressible fluid at high Reynolds number. *J. Fluid Mech.* 13(1):82–85
- Kubie J, Gardner G. 1977. Drop sizes and drop dispersion in straight horizontal tubes and in helical coils. *Chem. Eng. Sci.* 32(2):195–202
- Lalanne B, Masbernat O, Risso F. 2019. A model for drop and bubble breakup frequency based on

- turbulence spectra. *AIChE J.* 65(1):347–359
- Lamb H. 1879. Hydrodynamics. University Press, sixth ed.
- Lance M, Bataille J. 1991. Turbulence in the liquid phase of a uniform bubbly air–water flow. *J. Fluid Mech.* 222:95–118
- Legendre D, Magnaudet J. 1998. The lift force on a spherical bubble in a viscous linear shear flow. *J. Fluid Mech.* 368:81–126
- Legendre D, Zenit R, Velez-Cordero JR. 2012. On the deformation of gas bubbles in liquids. *Phys. Fluids* 24(4):043303
- Levich VG. 1962. Physicochemical Hydrodynamics. Prentice-Hall Inc.
- Liu HR, Ng CS, Chong KL, Lohse D, Verzicco R. 2021. An efficient phase-field method for turbulent multiphase flows. *J. Comput. Phys.* 446:110659
- Lohse D. 2018. Bubble puzzles: from fundamentals to applications. *Phys. Rev. Fluids* 3(11):110504
- Lu J, Fernández A, Tryggvason G. 2005. The effect of bubbles on the wall drag in a turbulent channel flow. *Phys. Fluids* 17(9):095102
- Lu J, Tryggvason G. 2008. Effect of bubble deformability in turbulent bubbly upflow in a vertical channel. *Phys. Fluids* 20(4):040701
- Ma T, Santarelli C, Ziegenhein T, Lucas D, Fröhlich J. 2017. Direct numerical simulation-based Reynolds-averaged closure for bubble-induced turbulence. *Phys. Rev. Fluids* 2(3):034301
- Maaß S, Kraume M. 2012. Determination of breakage rates using single drop experiments. *Chem. Eng. Sci.* 70:146–164
- Mac Huang J, Moore MNJ, Ristroph L. 2015. Shape dynamics and scaling laws for a body dissolving in fluid flow. *J. Fluid Mech.* 765:R3
- Machicoane N, Bonaventure J, Volk R. 2013. Melting dynamics of large ice balls in a turbulent swirling flow. *Phys. Fluids* 25(12):125101
- Madavan N, Deutsch S, Merkle C. 1985. Measurements of local skin friction in a microbubble-modified turbulent boundary layer. *J. Fluid Mech.* 156:237–256
- Maffettone P, Minale M. 1998. Equation of change for ellipsoidal drops in viscous flow. *J. Non-Newton. Fluid Mech.* 78(2-3):227–241
- Magnaudet J, Eames I. 2000. The motion of high-Reynolds-number bubbles in inhomogeneous flows. *Annu. Rev. Fluid Mech.* 32(1):659–708
- Mangani F, Soligo G, Roccon A, Soldati A. 2022. Influence of density and viscosity on deformation, breakage, and coalescence of bubbles in turbulence. *Phys. Rev. Fluids* 7(5):053601
- Maniero R, Masbernat O, Climent E, Risso F. 2012. Modeling and simulation of inertial drop break-up in a turbulent pipe flow downstream of a restriction. *Int. J. Multiph. Flow* 42:1–8
- Marchisio DL, Fox RO. 2013. Computational models for polydisperse particulate and multiphase systems. Cambridge University Press
- Marié JL, Grosjean N, Méès L, Seifi M, Fournier C, et al. 2014. Lagrangian measurements of the fast evaporation of falling diethyl ether droplets using in-line digital holography and a high-speed camera. *Exp. Fluids* 55(4):1–13
- Martínez-Bazán C, Montanes J, Lasheras JC. 1999. On the breakup of an air bubble injected into a fully developed turbulent flow. Part 1. breakup frequency. *J. Fluid Mech.* 401:157–182
- Mason TG, Wilking JN, Meleson K, Chang CB, Graves SM. 2006. Nanoemulsions: formation, structure, and physical properties. *J. Phys.: Condens. Matter* 18(41):R635
- Masuk AUM, Qi Y, Salibindla AK, Ni R. 2021a. Towards a phenomenological model on the deformation and orientation dynamics of finite-sized bubbles in both quiescent and turbulent media. *J. Fluid Mech.* 920:A4
- Masuk AUM, Salibindla A, Ni R. 2019a. A robust virtual-camera 3d shape reconstruction of deforming bubbles/droplets with additional physical constraints. *Int. J. Multiph. Flow* 120:103088
- Masuk AUM, Salibindla A, Tan S, Ni R. 2019b. V-ONSET (Vertical Octagonal Noncorrosive Stirred Energetic Turbulence): A vertical water tunnel with a large energy dissipation rate to study bubble/droplet deformation and breakup in strong turbulence. *Rev. Sci. Instrum.* 90(8):085105

- Masuk AUM, Salibindla AK, Ni R. 2021b. The orientational dynamics of deformable finite-sized bubbles in turbulence. *J. Fluid Mech.* 915:A79
- Masuk AUM, Salibindla AK, Ni R. 2021c. Simultaneous measurements of deforming hinze-scale bubbles with surrounding turbulence. *J. Fluid Mech.* 910:A21
- Mathai V, Lohse D, Sun C. 2020. Bubbly and buoyant particle-laden turbulent flows. *Annu. Rev. Condens. Matter Phys.* 11:529–559
- Mèès L, Grosjean N, Marié JL, Fournier C. 2020. Statistical Lagrangian evaporation rate of droplets released in a homogeneous quasi-isotropic turbulence. *Phys. Rev. Fluids* 5(11):113602
- Meneveau C, Sreenivasan K. 1991. The multifractal nature of turbulent energy dissipation. *J. Fluid Mech.* 224:429–484
- Mercado JM, Gomez DC, Van Gils D, Sun C, Lohse D. 2010. On bubble clustering and energy spectra in pseudo-turbulence. *J. Fluid Mech.* 650:287–306
- Mougin G, Magnaudet J. 2001. Path instability of a rising bubble. *Phys. Rev. Lett.* 88(1):014502
- Mukherjee S, Safdari A, Shardt O, Kenjereš S, Van den Akker HE. 2019. Droplet–turbulence interactions and quasi-equilibrium dynamics in turbulent emulsions. *J. Fluid Mech.* 878:221–276
- Murai Y. 2014. Frictional drag reduction by bubble injection. *Exp. Fluids* 55(7):1–28
- Murai Y, Fukuda H, Oishi Y, Kodama Y, Yamamoto F. 2007. Skin friction reduction by large air bubbles in a horizontal channel flow. *Int. J. Multiph. Flow* 33(2):147–163
- Oishi Y, Murai Y. 2014. Horizontal turbulent channel flow interacted by a single large bubble. *Exp. Therm. Fluid Sci.* 55:128–139
- Pal S, Merkle C, Deutsch S. 1988. Bubble characteristics and trajectories in a microbubble boundary layer. *The Phys. Fluids* 31(4):744–751
- Pandey V, Mitra D, Perlekar P. 2022. Turbulence modulation in buoyancy-driven bubbly flows. *J. Fluid Mech.* 932:A19
- Perlekar P, Benzi R, Clercx HJ, Nelson DR, Toschi F. 2014. Spinodal decomposition in homogeneous and isotropic turbulence. *Phys. Rev. Lett.* 112(1):014502
- Poorte R, Biesheuvel A. 2002. Experiments on the motion of gas bubbles in turbulence generated by an active grid. *J. Fluid Mech.* 461:127–154
- Prakash V, Tagawa Y, Calzavarini E, Mercado J, Toschi F, et al. 2012. How gravity and size affect the acceleration statistics of bubbles in turbulence. *New J. Phys.* 14(10):105017
- Qi Y, Masuk AUM, Ni R. 2020. Towards a model of bubble breakup in turbulence through experimental constraints. *Int. J. Multiph. Flow* 132:103397
- Qi Y, Tan S, Corbitt N, Urbanik C, Salibindla AK, Ni R. 2022. Fragmentation in turbulence by small eddies. *Nat. Commun.* 13(1):1–8
- Qian D, McLaughlin J, Sankaranarayanan K, Sundaresan S, Kontomaris K. 2006. Simulation of bubble breakup dynamics in homogeneous turbulence. *Chem. Eng. Commun.* 193(8):1038–1063
- Ravelet F, Colin C, Risso F. 2011. On the dynamics and breakup of a bubble rising in a turbulent flow. *Phys. Fluids* 23(10):103301
- Ravichandar K, Vigil RD, Fox RO, Nachtigall S, Daiss A, et al. 2022. Turbulent droplet breakage in a von kármán flow cell. *Phys. Fluids* 34(7):073319
- Riboux G, Risso F, Legendre D. 2010. Experimental characterization of the agitation generated by bubbles rising at high Reynolds number. *J. Fluid Mech.* 643:509–539
- Risso F. 2018. Agitation, mixing, and transfers induced by bubbles. *Annu. Rev. Fluid Mech.* 50:25–48
- Risso F, Fabre J. 1997. Diffusive turbulence in a confined jet experiment. *J. Fluid Mech.* 337:233–261
- Risso F, Fabre J. 1998. Oscillations and breakup of a bubble immersed in a turbulent field. *J. Fluid Mech.* 372:323–355
- Rivière A, Mostert W, Perrard S, Deike L. 2021. Sub-hinze scale bubble production in turbulent bubble break-up. *J. Fluid Mech.* 917:A40
- Roccon A, De Paoli M, Zonta F, Soldati A. 2017. Viscosity-modulated breakup and coalescence of large drops in bounded turbulence. *Phys. Rev. Fluids* 2(8):083603

- Rosti ME, Ge Z, Jain SS, Dodd MS, Brandt L. 2019. Droplets in homogeneous shear turbulence. *J. Fluid Mech.* 876:962–984
- Rushton J. 1950. Power characteristics of mixing impellers part 1. *Chem. Eng. Prog.* 46:395–404
- Russo E, Kuerten JG, Van Der Geld C, Geurts BJ. 2014. Water droplet condensation and evaporation in turbulent channel flow. *J. Fluid Mech.* 749:666–700
- Ruth DJ, Aiyer AK, Rivière A, Perrard S, Deike L. 2022. Experimental observations and modelling of sub-hinze bubble production by turbulent bubble break-up. *J. Fluid Mech.* 951:A32
- Ruth DJ, Vernet M, Perrard S, Deike L. 2021. The effect of nonlinear drag on the rise velocity of bubbles in turbulence. *J. Fluid Mech.* 924:A2
- Salibindla AK, Masuk AUM, Ni R. 2021. Experimental investigation of the acceleration statistics and added-mass force of deformable bubbles in intense turbulence. *J. Fluid Mech.* 912:A50
- Salibindla AK, Masuk AUM, Tan S, Ni R. 2020. Lift and drag coefficients of deformable bubbles in intense turbulence determined from bubble rise velocity. *J. Fluid Mech.* 894:A20
- Sanders WC, Winkel ES, Dowling DR, Perlin M, Ceccio SL. 2006. Bubble friction drag reduction in a high-Reynolds-number flat-plate turbulent boundary layer. *J. Fluid Mech.* 552:353–380
- Scapin N, Dalla Barba F, Lupo G, Rosti ME, Duwig C, Brandt L. 2022. Finite-size evaporating droplets in weakly compressible homogeneous shear turbulence. *J. Fluid Mech.* 934:A15
- Scarbolo L, Bianco F, Soldati A. 2015. Coalescence and breakup of large droplets in turbulent channel flow. *Phys. Fluids* 27(7):073302
- Scarbolo L, Molin D, Perlekar P, Sbragaglia M, Soldati A, Toschi F. 2013. Unified framework for a side-by-side comparison of different multicomponent algorithms: Lattice boltzmann vs. phase field model. *J. Comput. Phys.* 234:263–279
- Schultz S, Wagner G, Urban K, Ulrich J. 2004. High-pressure homogenization as a process for emulsion formation. *Chem. Eng. Technol.* 27(4):361–368
- Schuster S, Bernewitz R, Guthausen G, Zapp J, Greiner AM, et al. 2012. Analysis of w1/o/w2 double emulsions with clsm: Statistical image processing for droplet size distribution. *Chem. Eng. Sci.* 81:84–90
- Sevik M, Park S. 1973. The splitting of drops and bubbles by turbulent fluid flow. *J. Fluids Eng.* 95(1):53–60
- Shao C, Jin T, Luo K. 2022. The interaction between droplet evaporation and turbulence with interface-resolved direct numerical simulation. *Phys. Fluids* 34(7):072102
- Shiea M, Buffo A, Vanni M, Marchisio D. 2020. Numerical methods for the solution of population balance equations coupled with computational fluid dynamics. *Annu. Rev. Chem. Biomol. Eng.* 11:339–366
- Shinnar R. 1961. On the behaviour of liquid dispersions in mixing vessels. *J. Fluid Mech.* 10(2):259–275
- Soligo G, Roccon A, Soldati A. 2019. Breakage, coalescence and size distribution of surfactant-laden droplets in turbulent flow. *J. Fluid Mech.* 881:244–282
- Solsvik J, Jakobsen HA. 2015. Single air bubble breakup experiments in stirred water tank. *Int. J. Chem. React. Eng.* 13(4):477–491
- Solsvik J, Jakobsen HA. 2016. A review of the statistical turbulence theory required extending the population balance closure models to the entire spectrum of turbulence. *AIChE J.* 62(5):1795–1820
- Spandan V, Lohse D, Verzicco R. 2016. Deformation and orientation statistics of neutrally buoyant sub-Kolmogorov ellipsoidal droplets in turbulent Taylor-Couette flow. *J. Fluid Mech.* 809:480–501
- Spandan V, Verzicco R, Lohse D. 2018. Physical mechanisms governing drag reduction in turbulent Taylor-Couette flow with finite-size deformable bubbles. *J. Fluid Mech.* 849:R3
- Spelt P, Biesheuvel A. 1997. On the motion of gas bubbles in homogeneous isotropic turbulence. *J. Fluid Mech.* 336:221–244
- Sridhar G, Katz J. 1995. Drag and lift forces on microscopic bubbles entrained by a vortex. *Phys. Fluids* 7(2):389–399

- Stone HA. 1994. Dynamics of drop deformation and breakup in viscous fluids. *Annu. Rev. Fluid Mech.* 26(1):65–102
- Sugrue RM. 2017. A robust momentum closure approach for multiphase computational fluid dynamics applications. Ph.D. thesis, Massachusetts Institute of Technology. Department of Nuclear Science and Engineering
- Takagi S, Matsumoto Y. 2011. Surfactant effects on bubble motion and bubbly flows. *Annu. Rev. Fluid Mech.* 43:615–636
- Tan S, Salibindla A, Masuk AUM, Ni R. 2020. Introducing openlpt: new method of removing ghost particles and high-concentration particle shadow tracking. *Exp. Fluids* 61:1–16
- Tan S, Xu X, Qi Y, Ni R. 2023. Scalings and decay of homogeneous, nearly isotropic turbulence behind a jet array. *Phys. Rev. Fluids* 8(2):024603
- Tanaka T, Oishi Y, Park HJ, Tasaka Y, Murai Y, Kawakita C. 2021. Repetitive bubble injection promoting frictional drag reduction in high-speed horizontal turbulent channel flows. *Ocean Eng.* 239:109909
- Tanaka T, Oishi Y, Park HJ, Tasaka Y, Murai Y, Kawakita C. 2022. Frictional drag reduction caused by bubble injection in a turbulent boundary layer beneath a 36-m-long flat-bottom model ship. *Ocean Eng.* 252:111224
- Tomiya A, Tamai H, Zun I, Hosokawa S. 2002. Transverse migration of single bubbles in simple shear flows. *Chem. Eng. Sci.* 57(11):1849–1858
- Trefftz-Posada P, Ferrante A. 2023. On the interaction of Taylor length-scale size droplets and homogeneous shear turbulence. *J. Fluid Mech.*
- Tripathi MK, Sahu KC, Govindarajan R. 2015. Dynamics of an initially spherical bubble rising in quiescent liquid. *Nat. Commun.* 6(1):1–9
- Tryggvason G, Dabiri S, Aboulhasanzadeh B, Lu J. 2013. Multiscale considerations in direct numerical simulations of multiphase flows. *Phys. Fluids* 25(3):031302
- van den Berg TH, van Gils DP, Lathrop DP, Lohse D. 2007. Bubbly turbulent drag reduction is a boundary layer effect. *Phys. Rev. Lett.* 98(8):084501
- van Gils DP, Bruggert GW, Lathrop DP, Sun C, Lohse D. 2011. The Twente turbulent Taylor-Couette (T³C) facility: strongly turbulent (multiphase) flow between two independently rotating cylinders. *Rev. Sci. Instrum.* 82(2):025105
- van Gils DP, Guzman DN, Sun C, Lohse D. 2013. The importance of bubble deformability for strong drag reduction in bubbly turbulent Taylor-Couette flow. *J. Fluid Mech.* 722:317–347
- Vankova N, Tcholakova S, Denkov ND, Vulchev VD, Danner T. 2007. Emulsification in turbulent flow: 2. breakage rate constants. *J. Colloid Interface Sci.* 313(2):612–629
- Vejražka J, Zedníková M, Stanovský P. 2018. Experiments on breakup of bubbles in a turbulent flow. *AIChE J.* 64(2):740–757
- Vela-Martín A, Avila M. 2021. Deformation of drops by outer eddies in turbulence. *J. Fluid Mech.* 929:A38
- Vela-Martín A, Avila M. 2022. Memoryless drop breakup in turbulence. *Sci. Adv.* 8(50):eabp9561
- Verschoof RA, Van Der Veen RC, Sun C, Lohse D. 2016. Bubble drag reduction requires large bubbles. *Phys. Rev. Lett.* 117(10):104502
- Villermaux E. 2007. Fragmentation. *Annu. Rev. Fluid Mech.* 39:419–446
- Villermaux E, Wang X, Deike L. 2022. Bubbles spray aerosols: certitudes and mysteries. *PNAS Nexus* 1(5):1–13
- Voth GA, Soldati A. 2017. Anisotropic particles in turbulence. *Annu. Rev. Fluid Mech.* 49:249–276
- Wang C, Yi L, Jiang L, Sun C. 2022. Turbulence drag modulation by dispersed droplets in Taylor-Couette flow: the effects of the dispersed phase viscosity. *J. Fluid Mech.* 952:A39
- Wang L, Maxey M. 1993. The motion of microbubbles in a forced isotropic and homogeneous turbulence. *Appl. Sci. Res.* 51(1-2):291–296
- Wang T, Wang J, Jin Y. 2003. A novel theoretical breakup kernel function for bubbles/droplets in a turbulent flow. *Chem. Eng. Sci.* 58(20):4629–4637

- Wang Z, Mathai V, Sun C. 2019. Self-sustained biphasic catalytic particle turbulence. *Nat. Commun.* 10(1):3333
- Wilkinson PM, Van Schayk A, Spronken JP, Van Dierendonck LL. 1993. The influence of gas density and liquid properties on bubble breakup. *Chem. Eng. Sci.* 48(7):1213–1226
- Wooster TJ, Golding M, Sanguansri P. 2008. Impact of oil type on nanoemulsion formation and ostwald ripening stability. *Langmuir* 24(22):12758–12765
- Xing C, Wang T, Guo K, Wang J. 2015. A unified theoretical model for breakup of bubbles and droplets in turbulent flows. *AIChE J.* 61(4):1391–1403
- Yi L, Toschi F, Sun C. 2021. Global and local statistics in turbulent emulsions. *J. Fluid Mech.* 912:A13
- Yi L, Wang C, Huisman SG, Sun C. 2023. Recent developments of turbulent emulsions in Taylor-Couette flow. *Phil. Trans. R. Soc. A.* 381(2243):20220129
- Yi L, Wang C, van Vuren T, Lohse D, Risso F, et al. 2022. Physical mechanisms for droplet size and effective viscosity asymmetries in turbulent emulsions. *J. Fluid Mech.* 951:A39
- Zenit R, Feng J. 2018. Hydrodynamic interactions among bubbles, drops, and particles in non-newtonian liquids. *Annu. Rev. Fluid Mech.* 50:505–534
- Zenit R, Magnaudet J. 2008. Path instability of rising spheroidal air bubbles: a shape-controlled process. *Phys. Fluids* 20(6):061702
- Zhang H, Yang G, Sayyar A, Wang T. 2020. An improved bubble breakup model in turbulent flow. *Chem. Eng. J.* 386:121484
- Zhang J, Ni MJ, Magnaudet J. 2021. Three-dimensional dynamics of a pair of deformable bubbles rising initially in line. part 1. moderately inertial regimes. *J. Fluid Mech.* 920:A16
- Zhong S, Ni R. 2023. On the breakup rate of bubbles and droplets: a compilation and evaluation of experimental data. *in preparation*